

Multi-wire proportional chambers

8.1 Principles of operation

Single-wire proportional counters are widely used for detection and energy loss measurement of ionizing radiation; their localization capability is, however, determined by the physical size of the counter. Although some attempts were made to assemble several wire counters within the same gas volume, there was a general belief that multi-wire structures would not work properly because of the large capacitance between parallel non-screened wires, causing the signal to spread to many wires, thereby frustrating localization attempts. It was the merit of Georges Charpak and collaborators in the late 1960s to recognize that the positive signals induced on all electrodes surrounding an anode involving the avalanche largely compensate the negative signals produced by capacitive coupling; this led to the conception and successful test of the first multi-wire proportional chamber (MWPC), shown in Figure 8.1 (Charpak *et al.*, 1968).

The detector consists of a set of thin, parallel and equally spaced anode wires, symmetrically placed between two cathode planes; Figure 8.2 gives a schematic cross section of the structure. The gas gaps are typically three or four times larger than the wire spacing, although thin-gap devices have been developed and successfully operated. When symmetric negative potentials are applied to the cathodes, the anodes being grounded, an electric field develops, as seen in the equi-potentials and field lines shown in Figure 8.3.

As in a proportional counter, electrons created in the gas volume by an ionizing event drift along the field lines approaching the high field region, close to the anode wires, where avalanche multiplication can occur. Figure 8.4 shows schematically the variation of the electric field along a direction perpendicular to the wire plane, for a typical MWPC structure; notice the extended region with uniform field in the drift gap, and the decrease of the field between wires.

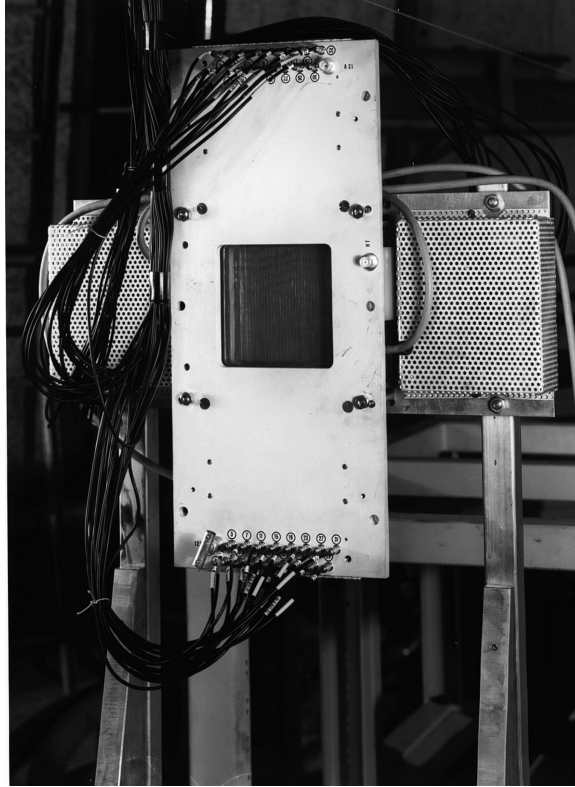


Figure 8.1 The first multi-wire proportional chamber, with 24 anode wires and $10 \times 10 \text{ cm}^2$ of active area. Picture CERN (1967).

Analytic expressions for the electric field can be obtained using standard electrostatic algorithms, and are given in many textbooks and articles (Morse and Feshbach, 1953; Durand, 1966; Erskine, 1972; Charpak, 1970). With the geometrical definitions of Figure 8.2:

$$V(x, y) = \frac{CV_0}{4\pi\epsilon_0} \left\{ \frac{2\pi l}{s} - \ln \left[4 \left(\sin^2 \frac{\pi x}{s} + \sinh^2 \frac{\pi y}{s} \right) \right] \right\}, \quad (8.1)$$

$$E(x, y) = \frac{CV_0}{2\pi \epsilon_0} \left(1 + \tan^2 \frac{\pi x}{s} \tanh^2 \frac{\pi y}{s} \right)^{\frac{1}{2}} \left(\tan^2 \frac{\pi x}{s} + \tanh^2 \frac{\pi y}{s} \right)^{-\frac{1}{2}}, \quad (8.2)$$

where V_0 is the voltage applied between anode and cathode planes, and the capacitance per unit length C is given by:

$$C = \frac{2\pi\epsilon_0}{\frac{\pi l}{s} - \ln \frac{2\pi a}{s}}, \quad (8.3)$$

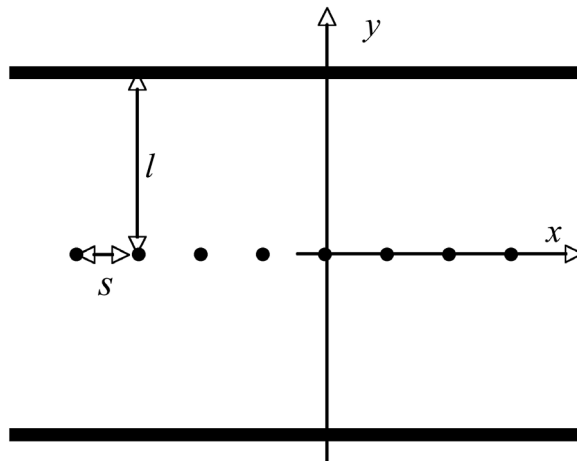


Figure 8.2 Schematics of the MWPC with definitions of the symbols used in the text.

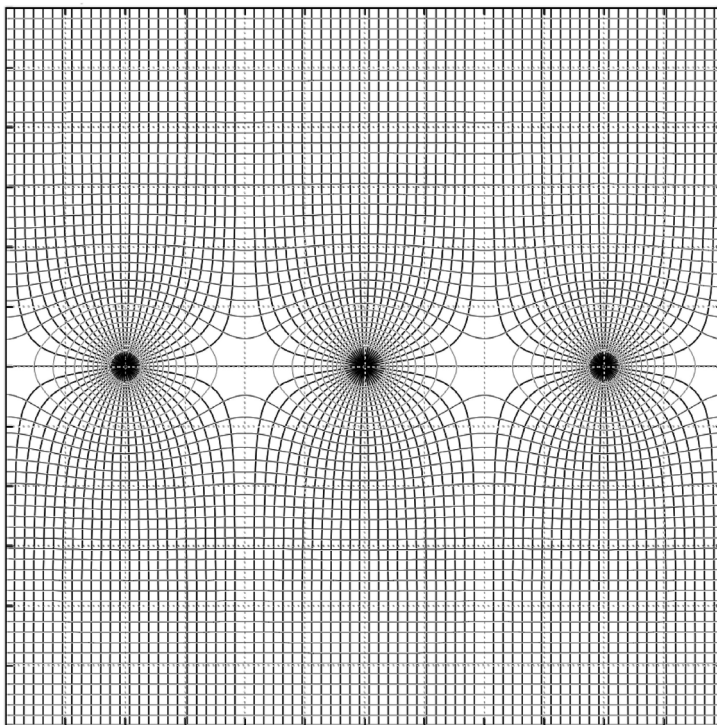


Figure 8.3 Field lines and equi-potentials near the anode wires in the MWPC.

Table 8.1 Capacitance per unit length (in pF/m) for several MWPC geometries.

<i>l</i> (mm)	<i>2a</i> (μm)	<i>s</i> (mm)			
		1	2	3	5
8	10	1.99	3.47	4.54	5.92
	20	2.04	3.63	4.55	6.39
	50	2.12	3.86	5.23	7.14
5	10	3.01	4.92	6.11	7.40
	20	3.13	5.24	6.62	8.15
	50	3.30	5.73	7.43	9.42

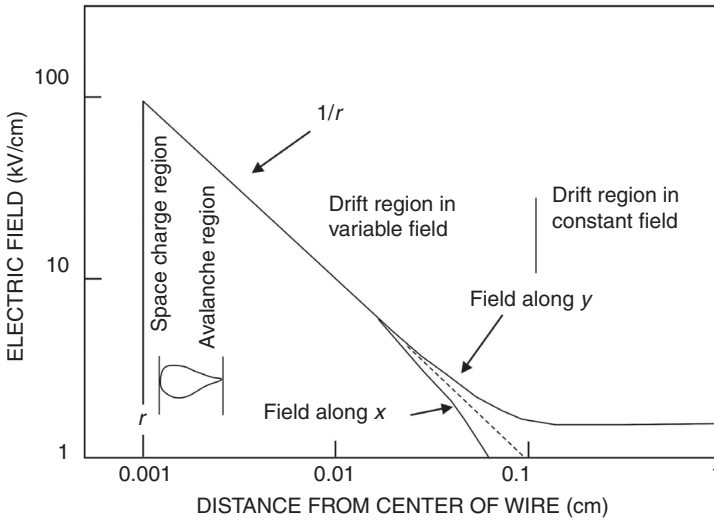


Figure 8.4 Electric field in the MWPC along the *x* and *y* directions.

where *a* is the anode wire radius. Note that, since $a \ll s$, the logarithm in the denominator is negative and the value given by expression (8.3) is always smaller than the capacity of the double plane condenser with the same surface ($2\pi\epsilon_0s/l$).

Computed values of the capacitance per unit wire length *C* are given in Table 8.1 for several MWPC geometries; the capacitance decreases with the wire spacing, while it depends little on the wire diameter.

Along the symmetry lines $x = 0$ and $y = 0$ the electric field is:

$$\begin{aligned}
 E_y = E(0, y) &= \frac{CV_0}{2\epsilon_0s} \coth \frac{\pi y}{s}, \\
 E_x = E(x, 0) &= \frac{CV_0}{2\epsilon_0s} \cot \frac{\pi x}{s}.
 \end{aligned}
 \tag{8.4}$$

It is instructive to consider the following approximations:

$$y \ll s : E(x, y) \approx \frac{CV_0}{2\pi\epsilon_0} \frac{1}{r} \quad r = \sqrt{x^2 + y^2}, \quad (8.5)$$

$$y \geq s : E_y \approx \frac{CV_0}{2\epsilon_0 s}. \quad (8.6)$$

Expression (8.5) shows that the field is radial around the anode, as in a cylindrical proportional counter; the results obtained in Sections 6.2 and 6.3 can then be used to estimate the operational characteristics of a multi-wire proportional chamber, provided that the correct value for the capacitance per unit length is used. In the drift region, the field is uniform and smaller than the parallel gap value V_0/l .

8.2 Choice of geometrical parameters

The anode wire distance determines the localization accuracy in a multi-wire chamber with digital readout; spacing below 2 mm is, however, difficult to realize and operate. One can understand the reasons by inspecting the expressions for the fields (8.5) and (8.6), and the approximate multiplication factor in a proportional counter (expression (7.7)). For a fixed wire diameter, to obtain a given gain one has to keep the charge per unit length CV_0 constant, i.e. increase V_0 when s (and therefore Q) is decreased; for example, going from 2 to 1 mm spacing, V_0 has to be almost doubled (see Table 8.1). The electric field in the drift region is also doubled; the probability of a breakdown is strongly increased. Practical experience has shown that, if a chamber with 2 mm wire spacing is relatively easy to operate, 1 mm spacing chambers are hard to manufacture and operate even for small sizes. Decreasing the wire diameters helps, but this brings in mechanical and electrostatic stability problems, see Section 8.4. Down-scaling all geometrical parameters (distance and diameter of the wires and gap) is not sufficient to provide a good operation: indeed, the mean free path for ionization remains invariant, unless the gas pressure is correspondingly increased. Work in this direction has been carried out to obtain good accuracies over small areas.

The approximate expression (7.7) for the gain of a cylindrical counter, using the values for the capacitance per unit length given in Table 8.1, permits one to investigate qualitatively the influence on gain of the wire diameter for a given MWPC geometry (Sauli, 1977). Figure 8.5 shows how the gain varies, as a function of the ratio V_0/V_T , for a MWPC with $s = 2$ mm, $l = 8$ mm and several anode wire radii. Although in principle any wire diameter allows one to obtain the desired gain, the steeper slope for large diameters implies a more critical operation when taking into account mechanical and electrical tolerances (see the next

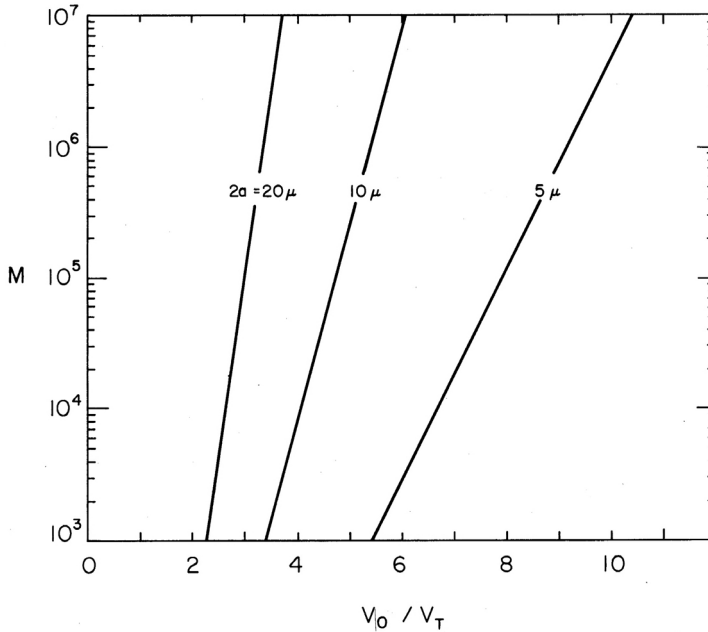


Figure 8.5 Gain dependence from voltage for a MWPC with several anode wire diameters (Sauli, 1977). By kind permission of CERN.

section). On the other hand, thicker anode wires are easier to handle, and a compromise has to be found; diameters around $10 \mu\text{m}$ are a practical lower limit, while $20 \mu\text{m}$ or larger are more frequently used.

8.3 Influence on gain of mechanical tolerances

The gain of a chamber at a given operational voltage depends on the detailed shape and value of the electric field in the multiplication region and can therefore change along a wire or from wire to wire as a consequence of mechanical variations. The maximum tolerable differences in gain depend on the specific application: in pulse-height measuring devices, requirements are much more severe than in threshold-operated chambers.

A detailed analysis of the gain variations due to different sources of mechanical tolerances can be found in Erskine (1972). Approximate estimates can be obtained again by making use of expression (7.7) for the multiplication factor (Sauli, 1977). By differentiation one gets:

$$\frac{\Delta M}{M} = \ln M \frac{\Delta Q}{Q} \text{ with } Q = CV_0. \quad (8.7)$$

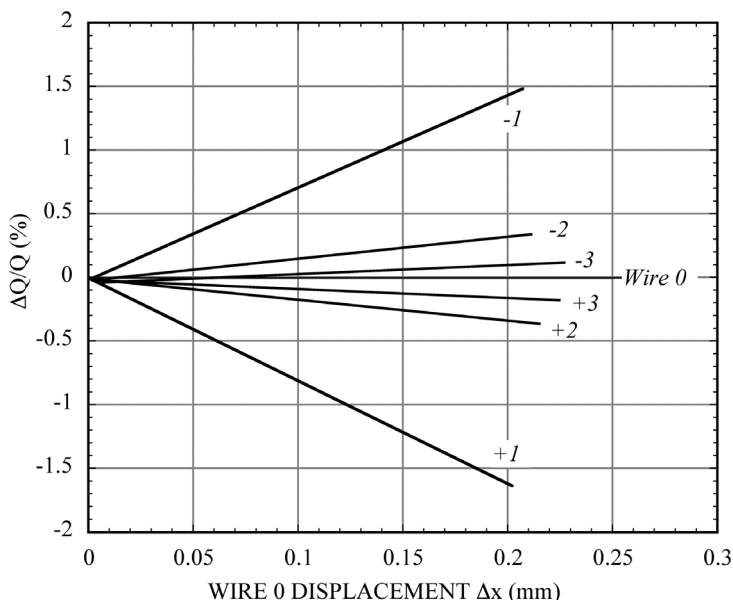


Figure 8.6 Relative charge change on adjacent wires due to wire 0 displaced in the x direction (Erskine, 1972). By kind permission of Elsevier.

The problem of gain variation is therefore reduced to a calculation of the change in the charge of the wires. From expression (8.3) for the capacitance per unit length C one can compute the effect of a change Δa in the wire radius and Δl in the gap:

$$\frac{\Delta Q}{Q} = \frac{C}{2\pi\epsilon_0} \frac{\Delta a}{a} \quad \text{and} \quad \frac{\Delta Q}{Q} = \frac{Cl}{2\pi\epsilon_0} \frac{\Delta l}{l}. \quad (8.8)$$

Consider, for example, a typical $l = 8$ mm, $s = 2$ mm chamber with $2a = 20$ μm operating at a gain of 10^5 . The approximate gain variations will be, from the previous expressions:

$$\frac{\Delta M}{M} \approx 0.8 \frac{\Delta a}{a} \quad \text{and} \quad \frac{\Delta M}{M} \approx 12 \frac{\Delta l}{l};$$

a typical diameter variation around $\sim 10\%$, as measured on standard 20 μm wires, results then in a $\sim 10\%$ change in gain, while a 1 mm difference in the gap thickness determines a $\sim 50\%$ gain change.

The displacement of a wire from the nominal position also results in a change of the charge per unit length for displaced wire as well as that of its neighbours. Computed for a standard MWPC geometry (2 mm wire spacing, 8 mm gaps and 20 μm wire diameter), Figure 8.6 and Figure 8.7 show the relative change in the charge per unit length of neighbouring wires, as a function of the displacement of a central wire

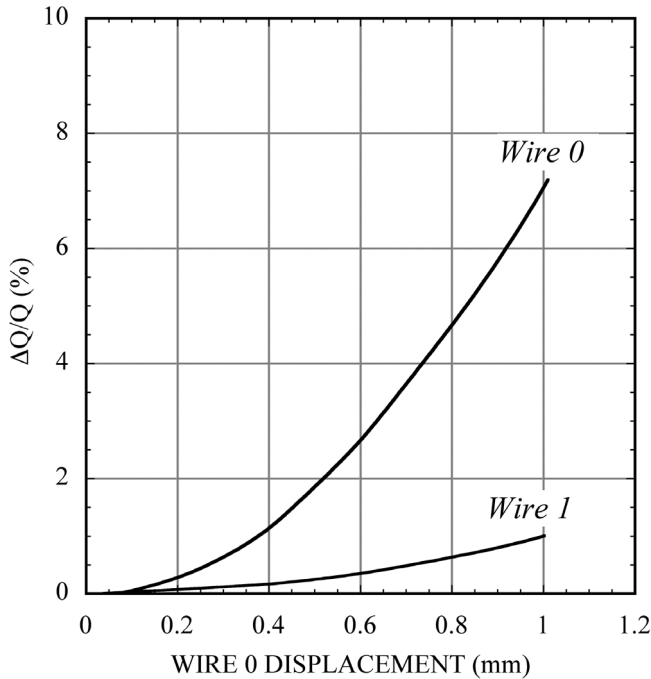


Figure 8.7 Relative charge change due to wire 0 displaced in the y direction (Erskine, 1972). By kind permission of Elsevier.

0 along the x and y directions (Erskine, 1972; Charpak, 1970).¹ A 10% (0.2 mm) displacement of a wire in the wire plane results in a 1.5% change in the charge of the two adjacent wires, and from (8.7), a 20% gain change at gains around 10^5 . This is obviously a critical parameter for the construction of multi-wire chambers.

Expression (8.7) can also be used to estimate the variation of the multiplication factor with the operational voltage V_0 ; a 1% change in V_0 results in an increase in relative gain of about 12% at $M = 10^5$. Experience shows that, with normal mechanical tolerances and for medium-size chambers, over-all gain variation around 20–30% can be expected over the active area, and this has to be taken into account when designing the detection electronics.

8.4 Electrostatic forces and wire stability

In a multi-wire structure, the anode wires are not in a stable equilibrium condition when a difference of potential is applied between anodes and cathodes. Indeed, if

¹ Note that in Figure 16 of the quoted reference the scale of the relative change for a wire displacement in the x direction is wrong by a factor of ten.

one wire is displaced from the middle plane, it is attracted more to the side of the displacement and less to the opposite, and the movement would continue indefinitely if there was no restoring force (the mechanical tension on the wires). It has been observed in large chambers that, above a certain value of the applied voltage, the wires become unstable, moving off the middle plane and reaching a new equilibrium with all wires alternately displaced towards the cathodes. Due to the reduction of the distance of the wires from the high voltage electrodes, a discharge may occur, propagating to the whole chamber and leading to spectacular failures, with most of the anode wires broken, as experienced in one of the first large MWPCs (Schilly *et al.*, 1970).

The critical length of a wire for stability can be computed from the balance of forces in the MWPC geometry (Trippe, 1969). Assuming the electric field to be radial, given by the approximate expression (8.5) and not modified by a small displacement δ off the median anode plane, the force per unit length between two equal linear charges CV_0 at a distance r is:

$$F(r) = \frac{(CV_0)^2}{2\pi\epsilon_0} \frac{1}{r};$$

approximating the tangents to the arcs, the total force per unit length on a given wire, in the direction normal to the wire plane, is:

$$\sum F_{\perp} = 2 \frac{(CV_0)^2}{2\pi\epsilon_0} \left[\frac{1}{s} \frac{2\delta}{s} + \frac{1}{3s} \frac{2\delta}{3s} + \dots \right] \approx \frac{\pi(CV_0)^2}{4\epsilon_0} \frac{\delta}{s^2}. \quad (8.9)$$

If T is the mechanical tension of the wire, the restoring force, in the direction perpendicular to the wire plane and per unit length, is:

$$R = T \frac{d^2\delta}{dx^2}.$$

$\delta = \delta(x)$ is the displacement of the wire along its length, with the conditions $\delta(0) = \delta(L) = 0$, where L is the wire length. At equilibrium, the restoring force should be equal and opposite to the force on the displaced wire, expression (8.9):

$$T \frac{d^2\delta}{dx^2} = - \frac{\pi(CV_0)^2}{4\epsilon_0} \frac{\delta}{s^2}.$$

The equation has the solution:

$$\delta(x) = \delta_0 \sin \left(\frac{CV_0}{2s} \sqrt{\frac{\pi}{\epsilon_0 T}} x \right),$$

and from the boundary condition $\delta(L) = 0$:

Table 8.2 Maximum tension before deformation for tungsten wires of different diameter.

$2a$ μm	T_M	
	N	g
5	0.04	4
10	0.16	16
20	0.65	66
30	1.45	146

$$\frac{CV_0}{2s} \sqrt{\frac{\pi}{\epsilon_0 T}} L \quad \text{or} \quad T = \frac{1}{4\pi\epsilon_0} \left(\frac{CV_0 L}{s} \right)^2.$$

For tensions larger than this value, no solution is possible other than $\delta(x) = 0$, implying that the wires remain stable. The required stability condition is, therefore:

$$T \geq T_C = \frac{1}{4\pi\epsilon_0} \left(\frac{CV_0 L}{s} \right)^2$$

or, if T_M is the maximum tension allowed by the elasticity module of a given wire, the critical stability length is:

$$L_C = \frac{s}{CV_0} \sqrt{4\pi\epsilon_0 T_M}. \quad (8.10)$$

Table 8.2 provides, for tungsten wires of several diameters, the maximum mechanical tension that can be applied before inelastic deformation.² For a MWPC with 2 mm spacing, 20 μm diameter tungsten wires and 8 mm gap, operated at 5 kV, expression (8.10) gives a maximum stable wire length of 90 cm. When larger detector sizes are needed, a mechanical support has to be used for the wires, at intervals shorter than the critical length (see Section 8.12).

Similar studies exist on the stability of cylindrical MWPCs (Bologna *et al.*, 1979), jet multi-wire chambers (Burckhart *et al.*, 1986) and single-wire drift tubes (Hammarström *et al.*, 1980b).

Another consequence of the electrostatic forces in a multi-wire chamber is the inward attraction of the outer electrodes towards the anode plane, and therefore an inflection of the cathode planes with a reduction of the gap width in the centre of a large chamber. Since the multiplication factor is rather sensitive to the gap width, this can be a problem for large chambers. Taking into account all charge distributions in the multi-wire chamber structure, one can compute the electrostatic force

² Mechanical wire tensions are often given in grams-weight (1 N = 102 g).

per unit surface, or pressure, on each cathode. For thin-foil electrodes, the deformation of the structure can then be estimated using standard mechanical tools, replacing weight with the electrostatic force.

An approximate estimate of the deflection can be obtained from expression (8.6) for the field in the drift volume. The field at the surface of the cathodes is:

$$E_s = \frac{E_y}{2} = \frac{CV_0}{4\epsilon_0 s};$$

simple charge balance shows then that the average charge per unit surface on each cathode is $CV_0/2s$, as can also be deduced from the expression taking into account the basic electrostatic relationship $E = \sigma/\epsilon_0$. The electrostatic pressure on each cathode is:

$$P = \frac{(CV_0)^2}{8\epsilon_0 s^2}. \quad (8.11)$$

The limits of validity of this expression can be found in the requirement that the field (and therefore the charge distribution) on the surface of the cathodes is constant; from inspection of Figure 8.3 one can see that this assumption holds for $l > s$.

The maximum inwards deflection of a square foil of side H , stretched with a linear tension T and subject to a pressure P , is then given by:

$$\Delta y = \frac{PH^2}{T} \frac{1}{8}. \quad (8.12)$$

Combining the two expressions, the maximum deflection for a given chamber geometry, or the maximum size for a chamber if a limit is set for the deflection, can be deduced. As an example, one can compute the maximum gap reduction in an $s = 2$ mm, 8 mm gap chamber with $H = 3$ m, operated at 4.5 kV. From Table 8.1, $CV_0 = 1.5 \times 10^{-6}$ C/m and, from (8.11), $P = 0.8$ N/m². For a typical aluminium foil electrode, 20 μ m thick, having a Young's modulus of 2×10^8 N/m², the maximum stretching tension T is 4×10^3 N/m; from (8.12) the maximum deflection is then 220 μ m, and the corresponding gain increase in the centre of the chamber is about 35% at gains of around 10^6 (see Section 6.3), in general not acceptable for correct operation. To reduce the gain non-uniformity, a mechanical gap-restoring support or spacer is necessary; several kinds of spacers and pillars have been developed but are a source of local inefficiency (see Section 8.12).

8.5 General operational characteristics: proportional and semi-proportional

A general discussion on gases used in proportional counters was given in Chapter 7; only a summary of experimental observations specific to multi-wire structures will be discussed here. A stable proportional or semi-proportional

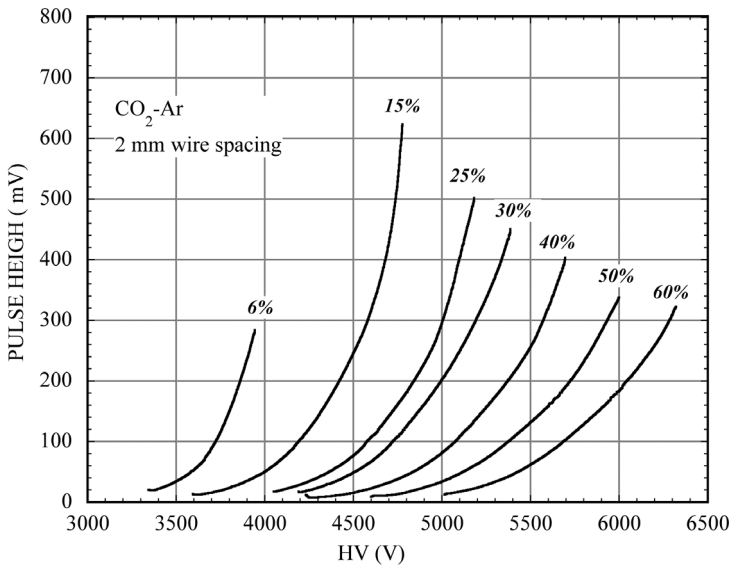


Figure 8.8 Peak pulse height measured on a MWPC on a 100 k Ω load for 5.9 keV X-rays as a function of voltage and for several argon–carbon dioxide mixtures (Bouclier *et al.*, 1970). By kind permission of Elsevier.

operation can be achieved in mixtures of a noble gas with a molecular gas having photon-quenching properties: carbon dioxide, hydrocarbons (methane, ethane, isobutane), ethylene, dimethylether, carbon tetrafluoride and many others. Gains around 10^5 can generally be obtained before breakdown. For the typical energy loss of fast particles in a thin gap of around 2 keV, this implies a total charge signal around 1 pC, or 100 mV on a 10 pF load (Table 2.1). Measured with a 2 mm wire spacing, 8 mm gap MWPC operated at atmospheric pressure, Figure 8.8 and Figure 8.9 show compilations of the average pulse height measured for ^{55}Fe 5.9 keV X-rays on a large load impedance (100 k Ω) for mixtures of argon–carbon dioxide and argon–isobutane (Bouclier *et al.*, 1970); curves stop at the appearance of discharges. Note the tendency to reach higher gains for mixtures containing 30–40% of quencher. For most applications, requiring a fast detector response, the total charge (that corresponds to the full collection of electrons and ions) is differentiated using a low load resistance, substantially reducing the signal amplitude (see the discussion in Section 7.3).

Recorded on 1 k Ω loads in similar conditions, Figure 8.10 shows the pulse-height distributions for 5.9 keV X-rays and minimum ionizing particles, having a most probable energy loss in the 2×8 mm gap filled with a 60–40 argon–isobutane mixture also around 6 keV: charged particles have the characteristic Landau distribution of pulse height; in both plots, the horizontal scale is 1 mV/division. Full detection efficiency for minimum ionizing particles can be obtained

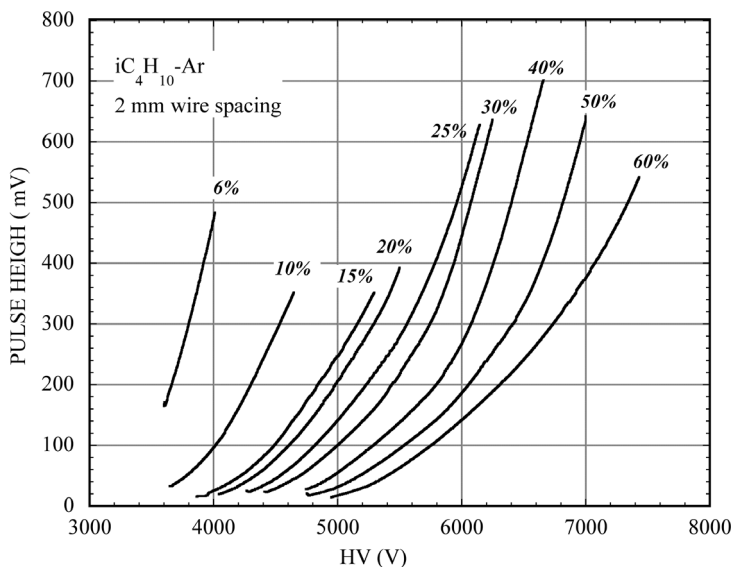


Figure 8.9 Peak pulse height measured on a MWPC on 100 k Ω load for 5.9 keV X-rays as a function of voltage and for several argon–isobutane mixtures (Bouclier *et al.*, 1970). By kind permission of Elsevier.

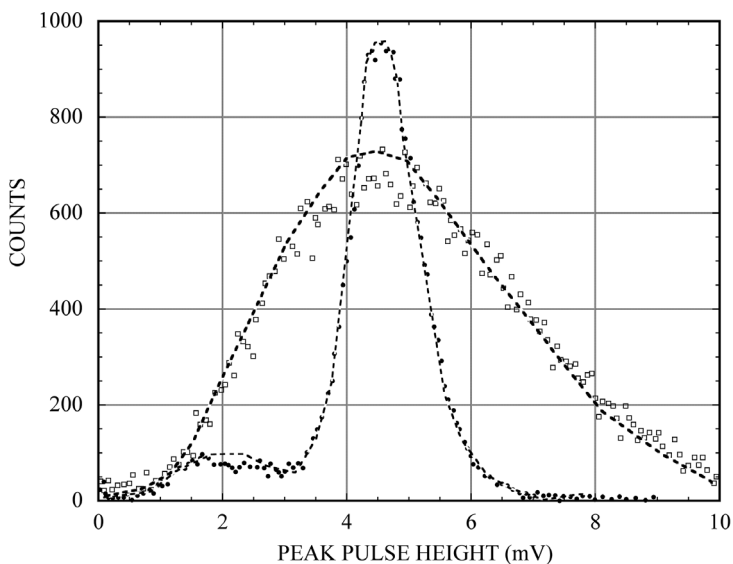


Figure 8.10 Pulse height spectra recorded in an 8 mm gap MWPC at the same voltage for 5.9 keV X-ray (the narrower peak) and minimum ionizing particles.

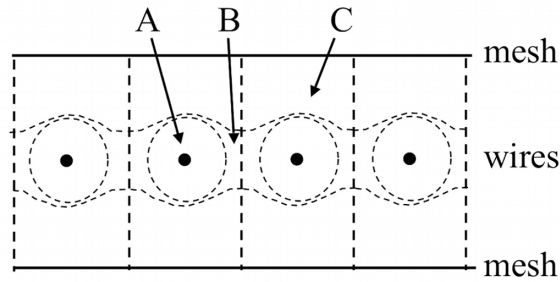


Figure 8.11 Schematics of the different regions of electrons collection around the wires.

with an electronic threshold around one tenth of the peak amplitude, or about 0.5 mV: this is a typical value for MWPC operation in the proportional region. The similarity of the two spectra explains the systematic use of the ^{55}Fe X-ray source for testing detectors designed for fast particle tracking.³

The timing properties of proportional chambers are determined by the collection time of the electrons produced by the ionizing tracks. The structure of the electric field around the wires allows the separation of three regions (Figure 8.11): electrons released in region A are quickly collected (typical drift velocities in these high fields are above 5 cm/ μsec). Tracks crossing the lower field region B between the wires, however, produce a characteristic tail in the time distribution; electrons created in the region C drift to the anode, where they are amplified and collected with a delay corresponding to the drift time. The time resolution of a chamber, defined as the minimum gate width necessary on the detection electronics for full efficiency, is of around 30 ns for a 2 mm spacing chamber. Figure 8.12 (left) shows a time distributions measured with all wires connected together, so that each track crosses region A or B of at least one wire, and corresponds to the intrinsic time resolution of the detector. Figure 8.12 (right) shows instead the time spectrum recorded on a single wire for an inclined beam: the long tail corresponds to tracks crossing the drift region C of this wire.

When detecting tracks not perpendicular to the chamber, the number of wires hit on each track (or cluster size) depends on the timing gate on the electronics; if the gate length is the minimum imposed by the requirement of full efficiency (around 30 ns), the cluster size will be of one or two wires in an angle-dependent ratio. If, on the other hand, the gate length corresponds to the maximum drift time from region C (about 200 ns for an 8 mm gap), the cluster size depends on the tracks' angle. Figure 8.13 shows the measured average cluster size for a large gate width

³ With the introduction of micro-pattern detectors, having narrower sensitive gaps, tests with the X-ray source tend to be optimistic.

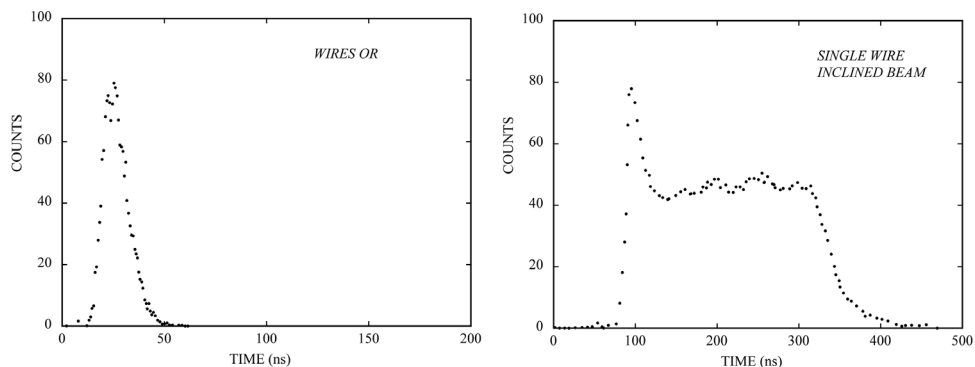


Figure 8.12 Time spectra recorded in a MWPC for minimum ionizing tracks. Left, with all wires connected together; right, for a single wire and an inclined beam.

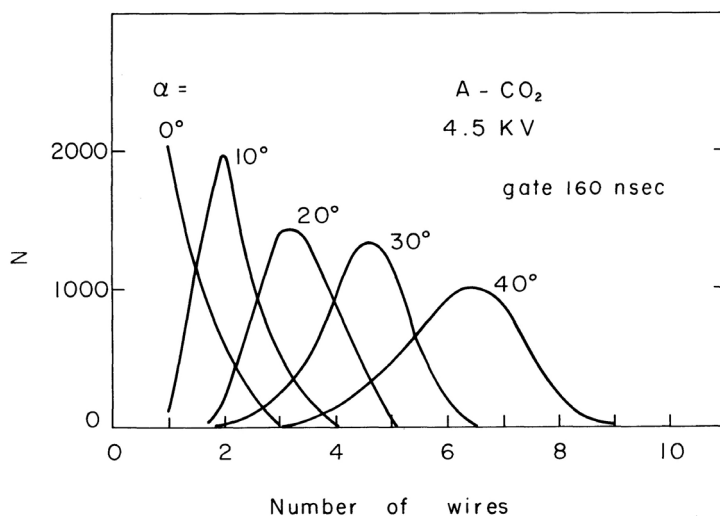


Figure 8.13 Cluster size for ionizing particle tracks at different incidence angles for a 2 mm pitch chamber (Bouclier *et al.*, 1970). By kind permission of Elsevier.

as a function of the angle of incidence ($\alpha = 0^\circ$ corresponds to tracks perpendicular to the wires' plane) (Bouclier *et al.*, 1970).

The detection efficiency of a MWPC depends on many parameters: amount and space distribution of the ionization released by radiation, gain of the detector, electronics threshold, time resolution; a low threshold allows one to get full efficiency at lower voltages, but is prone to be more sensitive to spurious signals due to input noise.

Efficiency and timing properties for charged particles are measured by exposing the detector to a charged particle beam and recording, with appropriate electronics,

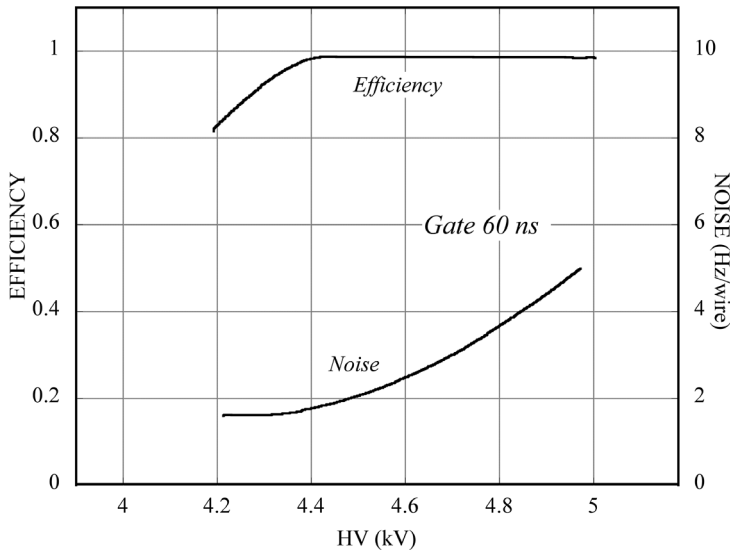


Figure 8.14 A typical efficiency and noise rate per wire measured with a large MWPC for fast particles (Charpak *et al.*, 1971). By kind permission of Elsevier.

the occurrence of pulses on wires above threshold in coincidence with an external geometrical and timing monitor (one or more scintillation counters). Figure 8.14 gives an example of the voltage dependence of detection efficiency for minimum ionizing particles, perpendicular to the chamber, measured in one of the first large MWPCs with 2 mm wire spacing; the singles counting rate, or noise per wire, is also shown in the figure (Charpak *et al.*, 1971). The efficiency depends on the coincidence gate width, as seen in Figure 8.15 (Schilly *et al.*, 1970) and on the electronics input discrimination threshold, Figure 8.16 (Duerdoth *et al.*, 1975).

For applications requiring X-ray detection, as for diffraction experiments from synchrotron radiation sources, xenon mixtures are preferred to provide higher detection efficiency. If a good energy resolution is also required, the operating voltage is a compromise between high gain and best resolution, as shown in Figure 8.17 and Figure 8.18 (Duerdoth *et al.*, 1975).

A comparative analysis of gas properties and of the criteria for a choice meeting the experimental requirements can be found in Va'vra (1992).

8.6 Saturated amplification region: Charpak's 'magic gas'

Presence in the gas mixture of electro-negative pollutants, like oxygen or halogens, results in the capture of electrons with the consequent loss of proportionality, and

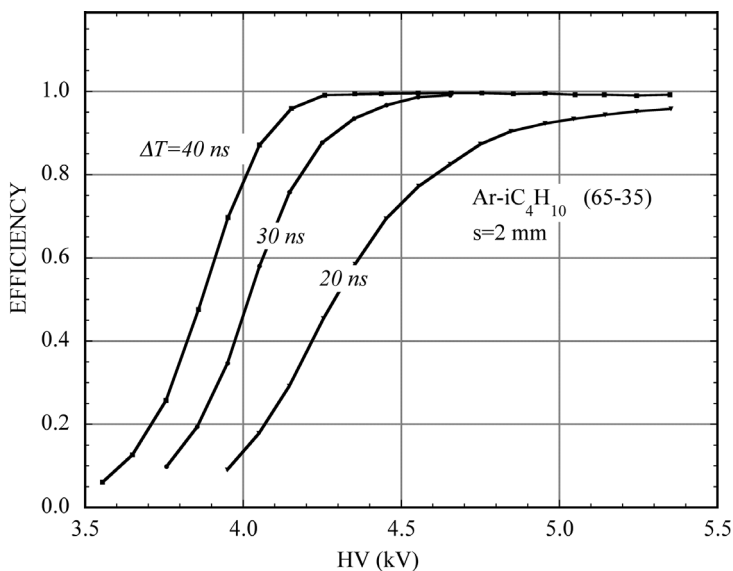


Figure 8.15 Efficiency as a function of voltage for several gate lengths (Schilly *et al.*, 1970). By kind permission of Elsevier.

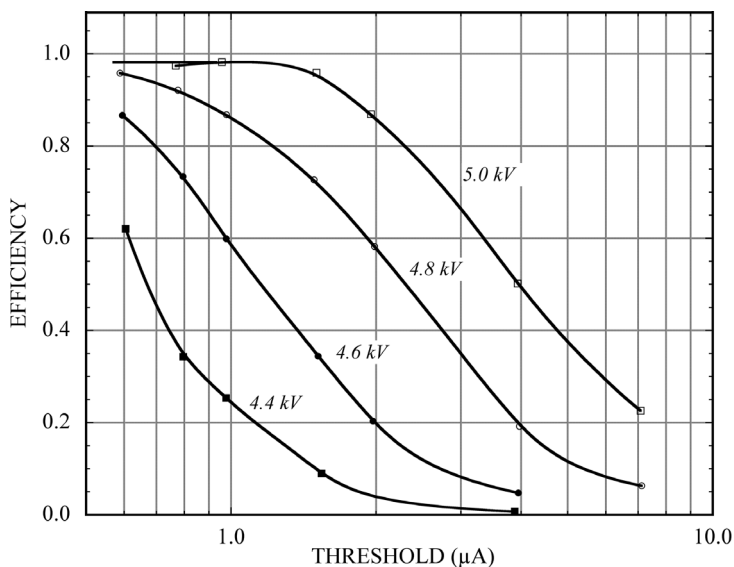


Figure 8.16 MWPC efficiency for fast particles as a function of the discrimination threshold and high voltage (Duerdoth *et al.*, 1975). By kind permission of Elsevier.

should in general be avoided. However, since the effective capture probability depends on the electrons' distance from the wires, the property can be exploited to restrict the sensitive region, thus reducing the dependence of the detected signals on the incidence angle of tracks. With 20% ethyl bromide (C₂H₅Br)

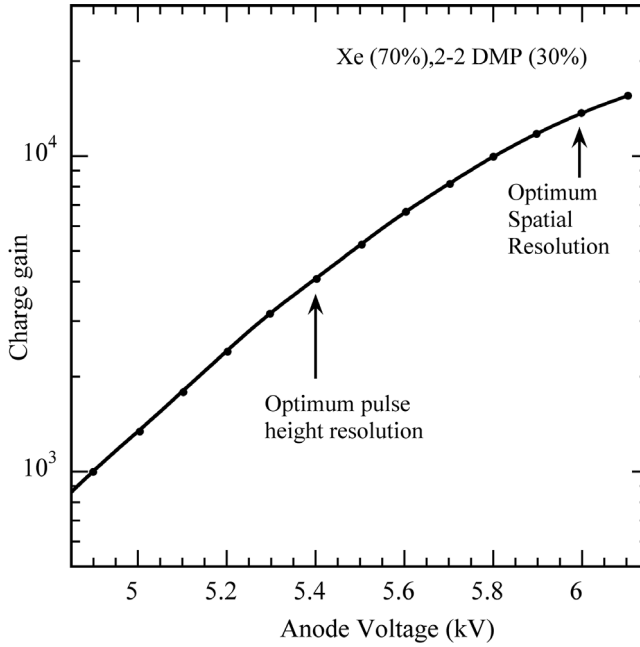


Figure 8.17 Gain of a 1 mm wire spacing chamber filled with xenon–dimethyl propane (Duerdoth *et al.*, 1975). By kind permission of Elsevier.

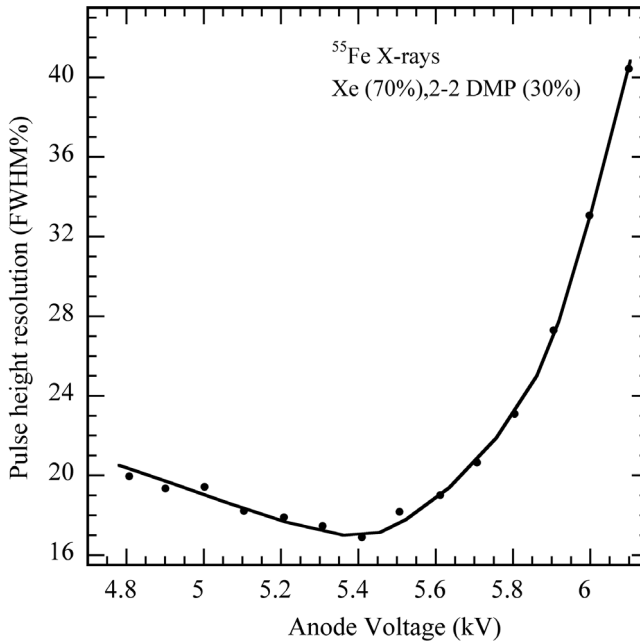


Figure 8.18 Energy resolution on 5.9 keV X-rays in a xenon–DMP filled chamber as a function of applied voltage (Duerdoth *et al.*, 1975). By kind permission of Elsevier.

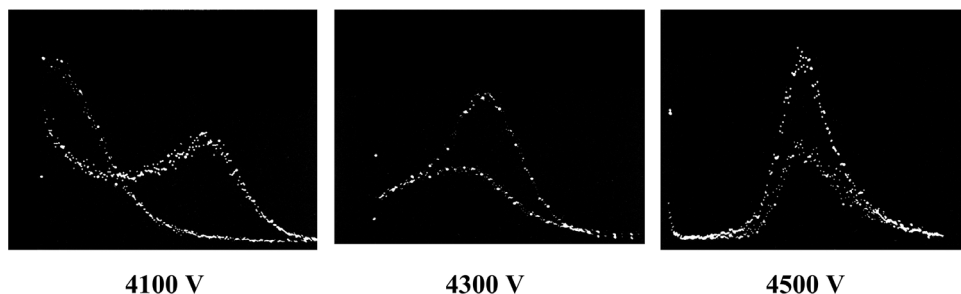


Figure 8.19 Pulse height spectra for 5.9 keV and fast particles recorded in magic gas at increasing voltages. The horizontal scale is adjusted to match the increasing pulse heights (Bouclier *et al.*, 1970). By kind permission of Elsevier.

added to the mixture, the sensitive region around the anode wires is reduced to about 1 mm, at the same time permitting one to reach high gains (Grunberg *et al.*, 1970).

As first noticed by Charpak and collaborators, addition of freon-13B1(CF₃Br) permits one to reach a fully saturated operation, i.e. a pulse-height distribution independent of the number of primary ionization charges (Bouclier *et al.*, 1970). The appearance of gain saturation in the so-called magic gas, argon–isobutane–freon in the volume proportions 70/29.6/0.4 is illustrated in Figure 8.19, showing pulse-height spectra for minimum ionizing electrons and 5.9 keV X-rays recorded at increasing voltages; owing to the large increase in the gain, the horizontal scales in the plots differ. Due to the presence of the electro-negative addition, spectra are degraded due to electron capture, but the evolution from a quasi-proportional to a fully saturated regime is apparent. Under these conditions, a single photoelectron provides fully saturated signals (Breidenbach *et al.*, 1973).

The amount of electro-negative gas that can be used in a chamber is limited by the requirement of full efficiency: the mean free path for electron capture, λ_C , should not be smaller than the wire spacing. Figure 8.20 shows the efficiency for a 2 mm wire spacing chamber measured at increasing concentrations of freon; under reasonable assumptions on the detection and capture mechanisms, the experimental points are well approximated by the relationship $\lambda_C = 0.63/p$, where p is the freon percentage and λ_C is given in mm (Breidenbach *et al.*, 1973).

An important consequence of the presence of an electro-negative gas in the mixture is a different dependence of the cluster size on the gate length; electrons produced in the drift region have a very small probability of reaching the anodes, and the cluster size is limited even for long gates.

The large amplitude and reduced dynamic range of saturated pulses, easing the electronics requirements, was essential in the early development of the technology

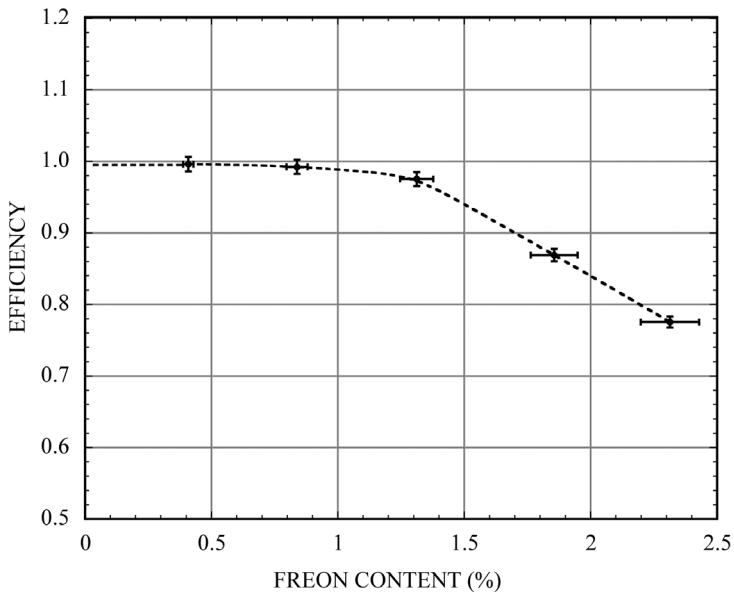


Figure 8.20 Efficiency for fast particles of a 2 mm pitch chamber as a function of freon content (Breidenbach *et al.*, 1973). By kind permission of Elsevier.

and has been adopted by many experiments (Bouclier *et al.*, 1974; Baksay *et al.*, 1976; Frieze *et al.*, 1976; Doll *et al.*, 1988).

The large, saturated gain features of the magic gas have been observed in other mixtures containing small percentages of freon, such as argon–methane and argon–ethane (Koori *et al.*, 1984; Koori *et al.*, 1986a); they should, however, not be confused with the very large signals obtained in the conditions where a transition to a self-quenching streamer is possible (see the next section).

The availability of low threshold highly integrated front-end electronics, and the moratorium on production of fluorinated gases due to ecological reasons have phased out the use of the ‘magic gas’.

8.7 Limited streamer and full Geiger operation

A peculiar mode of operation has been observed in proportional chambers having widely spaced thick wires and filled with small concentrations of organic quenchers: the appearance of very large signals in what was first attributed to a transition from proportional avalanches to a damped Geiger propagation, limited in spatial extension to around 10 mm along the wire (Brehin *et al.*, 1975). Although very attractive because of the large signal pulse height that could be obtained (30–40 mV on a 50 Ω load) this mode of operation has a severe rate limitation due

to the long time taken by the positive ion sheath to clear the concerned anode wire section. For an 8 mm gap chamber, the assumption that after each count a 10 mm long section of the wire is dead for about 300 μs provides a good agreement with the experimentally measured efficiency.

It was demonstrated later that the large signals were probably due to another mode of discharge, propagating perpendicular to the wires and stopping before reaching the cathodes; the process was appropriately named self-quenching streamers (SQS) (Alexeev *et al.*, 1980), and was confirmed by optical observation of the photons emitted by the avalanches (Atac and Tollestrup, 1982). This operational mode has been used for the limited streamer tube arrays, to be described in Section 12.1.

Full Geiger propagation along all the wire has also been observed in multi-wire chambers operated with a small percentage of organic quencher, like methylal or ethyl bromide added to pure argon, albeit with the long dead-times characteristic of this mode of operation. A measurement of the propagation time of the Geiger streamer along the wires has been used to provide two-dimensional images of the conversion points, making them suitable for low-rate neutral radiation imaging (Charpak and Sauli, 1971).

A large gain, saturated mode of operation has also been observed using heavily quenched gas mixtures in the so-called thin-gap chambers (TGC), developed for applications where the total thickness of the detector has to be minimized (Majewski *et al.*, 1983; Bella *et al.*, 1986). The detectors have been successfully used in the pre-sampling of the OPAL electro-magnetic calorimeter (Beard *et al.*, 1990) and the ATLAS muon spectrometer (Aloisio *et al.*, 2004), and are under development for a high-rate, large size upgrade of the muon tracker for the Super Large Hadron Collider (SLHC) (Amram *et al.*, 2011). In extended beam tests, the detectors have demonstrated reliable operation and resilience to radiation damage up to a large accumulated charge.

8.8 Discharges and breakdown: the Raether limit

The transition of the avalanche to a streamer, and the subsequent sudden appearance of discharges in uniform field counters were discussed in Section 5.5. The transition occurs when the total amount of charge in an avalanche exceed about 10^7 electron-ion pairs, the so-called Raether limit. In wire chambers, a proper choice of geometry and gas mixture permits the operation in the limited or self-quenching regimes, but on increasing the voltage further the conditions are met for full discharge propagation through the structure, often with irreversible damage. Methods of dumping the energy of a discharge by making use of resistive electrodes are discussed in Chapter 12.

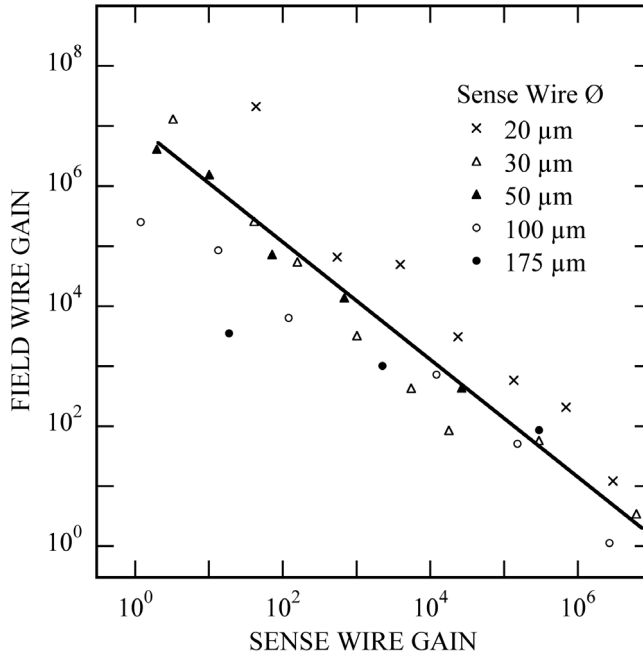


Figure 8.21 Correlation between measured gains of the anode and estimated gain of the cathode wires at discharge (Giubellino *et al.*, 1986). By kind permission of Elsevier.

In structures having non-planar cathodes (wires or strips) the critical Raether condition can be met at smaller apparent values of collected charge due to secondary emission from the high field regions in the cathode plane. A measurement of this effect is shown in Figure 8.21 (Giubellino *et al.*, 1986): in a detector having anode wires centred in a square wire cathode cell, the maximum gain at discharge for the anodes has been correlated to the gain of the cathodes, estimated from the gain the wire would have if used as anode, in a range of wire diameters. Electrons ejected from the cathode by secondary emission experience charge multiplication before getting to the anodes; the product of the two gains roughly corresponds to the Raether limit. Similar gain-limiting processes have been observed in micro-pattern gaseous detectors (see Chapter 13).

The presence of thin insulating layers on cathodes, either manufacturing residuals or created by the organic polymerization processes induced by the avalanches, described in Chapter 16, can also trigger a cascade of events leading to a discharge. Ions produced in the multiplication process can accumulate on the insulating layer, creating a high local dipole electric field; if this field exceeds a critical value, electrons can be extracted from the underlying metal electrode and

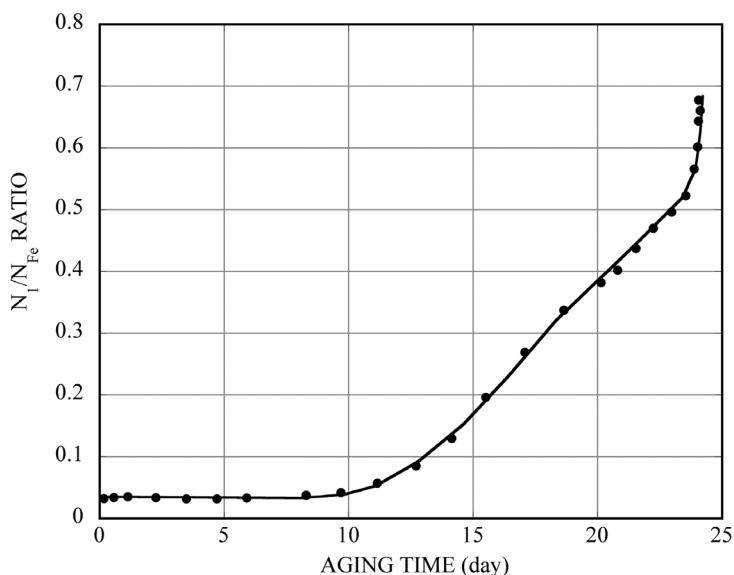


Figure 8.22 Normalized spontaneous single electron counting rate as a function of irradiation time (Boyarski, 2004). By kind permission of Elsevier.

injected into the gas gap, the so-called Malter effect (Malter, 1936). Drifting to the anode, the secondary electrons create more ions, and the process can diverge, leading to the condition of discharge.

A field-emission model taking into account the ions' accumulation and depletion rates on thin-film deposits has been developed and compared with the measured current spikes generated by field-emitted electrons for the specific conditions met in wire chambers (Boyarski, 2004). Figure 8.22 shows how the single electron counting rate, normalized to the source rate, increases with the irradiation time during an ageing test, until reaching the divergence condition; the full line is a fit of the model prediction to the experimental data.

Other breakdown mechanisms, involving long-term modifications of the charge distributions in counters, named 'cumulative' and attributed to a memory of previous occurrences in the detectors, have also been discussed (Ivanouchenkov *et al.*, 1999; Iacobaeus *et al.*, 2001).

Although not directly related to the breakdown mechanisms, an enhancement of spontaneous electron emission due to a decrease of the electronic work function on aluminium cathodes has been found to make gaseous detectors sensitive to visible light. As an example, Figure 8.23 compares the normal counting and the noise rate of a detector exposed to a radioactive source in darkness (upper plot) and in ambient light (lower plot) (Chirihov-Zorin and Pukhov, 1996).

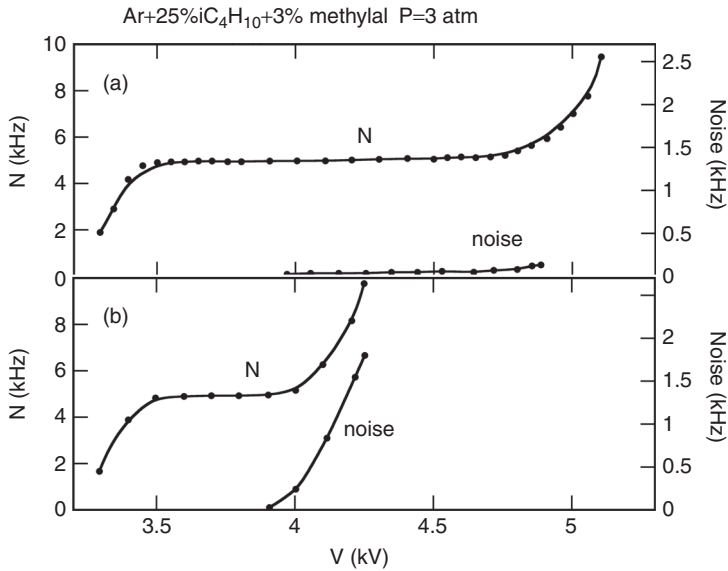


Figure 8.23 Counting and noise rates of a detector in the darkness (a) and exposed to light (b) (Chirihov-Zorin and Pukhov, 1996). By kind permission of Elsevier.

An increase of leakage current due to infra-red radiation, attributed to a person approaching the detector, was also curiously observed in the early developments of MWPCs, but remains anecdotal (Marsh *et al.*, 1979).

The survivability of a wire chamber to breakdowns depends on mechanical construction, energy and frequency of the discharges. Thin anode wires are obviously more prone to failure than thick wires or continuous electrodes. Although spark damages are a common occurrence during detectors' development and tests, only a few systematic studies have been reported on this matter. Figure 8.24 (Rotherburg and Walsh, 1993) is an example of measurements of the energy of a spark needed to break a 10 μ m tungsten wire stretched at increasing mechanical tensions; curves are the predictions of a simple model discussed in the reference.

Methods for reducing the discharge energy by sectoring the high-voltage electrodes, with individual high value protection resistors, or by making the electrodes themselves resistive, have been introduced in the development of the limited streamer tubes, resistive plate chambers and micro-pattern gas counters, and will be discussed in the following chapters.

8.9 Cathode induced signals

As noted in the introduction, the avalanche formation, fast electrons collection on the anodes and the ensuing backward motion of ions, result in a distribution of

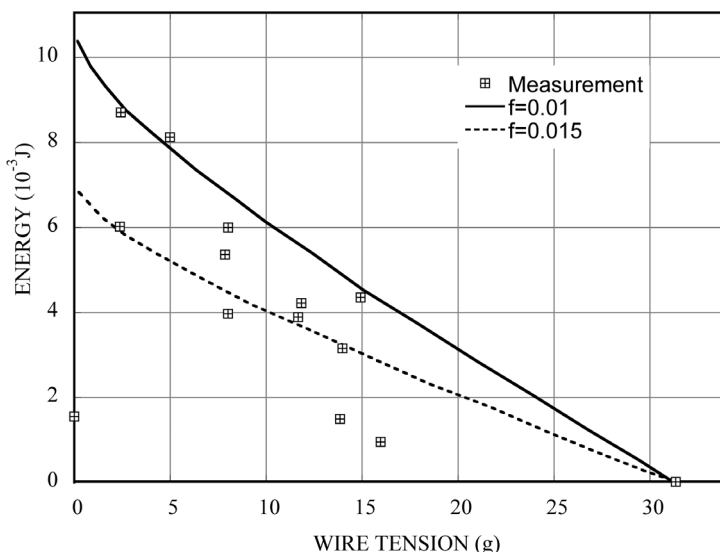


Figure 8.24 Energy of a spark needed to break a 10 μm wire as a function of wire tension (Rotherburg and Walsh, 1993). By kind permission of Elsevier.

induced positive charge on electrodes surrounding the wire, the adjacent wires and the cathodes. The possibility of exploiting a measurement of induced signals to obtain information on the position of the avalanche was discussed in the early works on MWPCs (Charpak *et al.*, 1970).

A simple signal over threshold detection on wide strips on the high voltage planes can be used to provide coarse information on the coordinates of the avalanche along the wires; Figure 8.25 is an efficiency scan through several adjacent cathode strips, 8 cm wide, for a collimated electron source (Fischer and Plch, 1972). The combined detection efficiency is close to 100%, but due to mutual cross talk some residual efficiency is measured for off-beam positions, which can be minimized by a thorough choice of operating conditions and discrimination threshold. A digital readout of wide strips on the cathode planes was used in the first large experimental setup using two-dimensional multi-wire chambers, and had the advantage of reducing the number of modules and mass of the tracker when compared to a solution deploying chambers with inclined wires (Bouclier *et al.*, 1974).

The process of cathode charge induction has been extensively analysed both experimentally and theoretically, particularly in view of its capability of two-dimensional and accurate localization of neutral events. In coincidence with the anode pulses or started by an external trigger, the positive induced charge profile is recorded on sets of readout electrodes on the high-voltage planes: groups of cathode wires or printed circuit strips, at angles with the anodes (Figure 8.26).

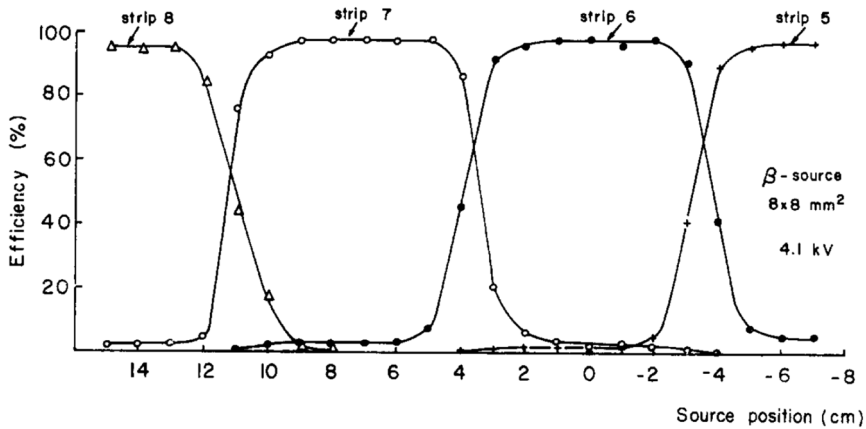


Figure 8.25 Efficiency scan through wide strips on the cathode plane (Fischer and Plch, 1972). By kind permission of Elsevier.

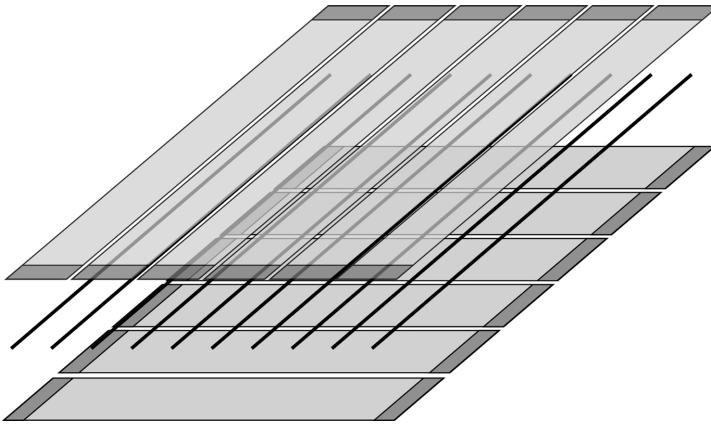


Figure 8.26 Schematics of a MWPC with readout of the cathode induced signals on two sets of perpendicular strips.

The coordinates are then deduced, in the simplest formulation, from a calculation of the centre-of-gravity (COG) of the recorded charge:

$$\bar{x} = \frac{\sum x_i X_i}{\sum X_i} \quad \text{and} \quad \bar{y} = \frac{\sum y_i Y_i}{\sum Y_i}, \quad (8.13)$$

where x_i (y_i) and X_i (Y_i) are respectively the central coordinate and the charge recorded on strip i for the projections along two coordinates x and y ; the weighted average is made on the set of adjacent strips having a detected signal above some pre-determined threshold. The space-COG correlation is almost linear for the coordinate y , along the

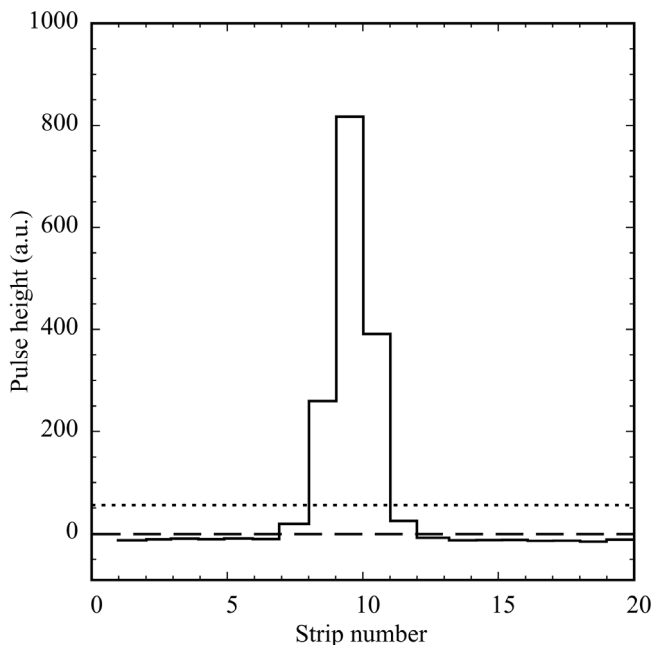


Figure 8.27 Induced charge distribution on cathodes of a 5 mm gap MWPC; the readout strip pitch is 5 mm. The dotted line indicates a bias value used in the analysis (Charpak *et al.*, 1979b). By kind permission of Elsevier.

anodes; under special conditions, to be discussed later, an exploitable non-linear correlation exists also for the coordinate x perpendicular to the wires.

Figure 8.27 is a measurement of a single event charge distribution recorded on cathode strips, 5 mm wide; the distribution has a quasi-Gaussian shape with a standard deviation close to the MWPC gap thickness of 5 mm (Charpak *et al.*, 1979b); this has become a standard rule of thumb for the cathode induction processes, discussed in detail in Section 10.4. For a modern formulation of the signal formation and induction in gaseous counters see Riegler (2004).

For the coordinate along the anode wires, a simple modification of the expression permits one to reduce the dispersive effect of noise and inter-strip cross talk, subtracting a constant bias level B to all measured charges:

$$\bar{s} = \frac{\sum (Q_i - B) s_i}{\sum (Q_i - B)}, \quad (8.14)$$

in which negative terms in the sum are neglected; a fit to the data provides the best estimate of the bias term B (Charpak *et al.*, 1979b). In a further refinement of the expression, choice of a bias level proportional to the measured amplitude,

$B = b\Sigma Q_i$ permits one to achieve, with a proper value of the parameter b , the best localization independently of the position of the source with respect to the strips (Figure 8.28) (Piuz *et al.*, 1982).

For charged particles, the angle of incidence to the detector plane plays a major role in determining the localization accuracy, due to asymmetric energy losses caused by delta electrons, as discussed in Section 2.4. A detailed analysis shows the correlation between localization and recorded energy loss for fast particles: while for normal incidence the position accuracy is almost independent of the pulse height, for inclined tracks the dispersion is considerably worse for large energy losses, confirming the crucial role of the delta electrons, Figure 8.29 (Charpak *et al.*, 1979b). The dispersive effect of long-range secondary electrons is manifest in the residual distribution measured with high-accuracy detectors for a perpendicular beam, shown in Figure 8.30. While the standard deviation of a Gaussian fit to the single detector resolution is 15 μm , large deviations in the tails due to delta electrons are clearly visible (Bondar *et al.*, 1983).⁴

For soft X-rays, and using a xenon-based gas mixture to reduce the physical path of the photoelectron in the gas, a localization accuracy of 35 μm rms for the coordinate along the wires could be achieved for a collimated soft X-ray source, Figure 8.31 (Charpak *et al.*, 1978).

The correlation between real position and COG measurement, continuous in the direction parallel to the anode wires, jumps through steps in the perpendicular direction, due to the discrete wire spacing. However, it was found in the early works that, at least at moderate proportional gains, the avalanche does not surround the anode, and the direction of the ions' backflow retains a memory of the original direction of approach of the ionization. The correlation between reconstructed GOG and real position is not linear, but can be unfolded with appropriate algorithms to obtain the space coordinate in the direction perpendicular to the wires, albeit not with the same accuracy as for the one along the anodes; the result can be improved further by a measurement of the induced charge on the two adjacent anode wires (Breskin *et al.*, 1977). Figure 8.32 is the image obtained by exposing a 2 mm spacing MWPC with 3 mm wide cathode strip readout to soft X-rays through a metal mask with letter cuttings $4 \times 1.5 \text{ mm}^2$ in size (Charpak *et al.*, 1978). Using the proper correlations, the centre of gravity method provides bi-dimensional localization with accuracy better than 100 μm .

The angular spread of the avalanche around the wires and its dependence on geometry, gas mixture and gain have been studied both experimentally and theoretically by many authors (Mathieson and Harris, 1979; Fischer *et al.*, 1978;

⁴ For charged particles, the space resolution is usually deduced from the calculation of the residuals, the difference between predicted and measured coordinates for three identical detectors; if σ_R is the standard deviation of the residuals, the single coordinate resolution is given by $\sigma_1 = \sigma_R/\sqrt{2}$.

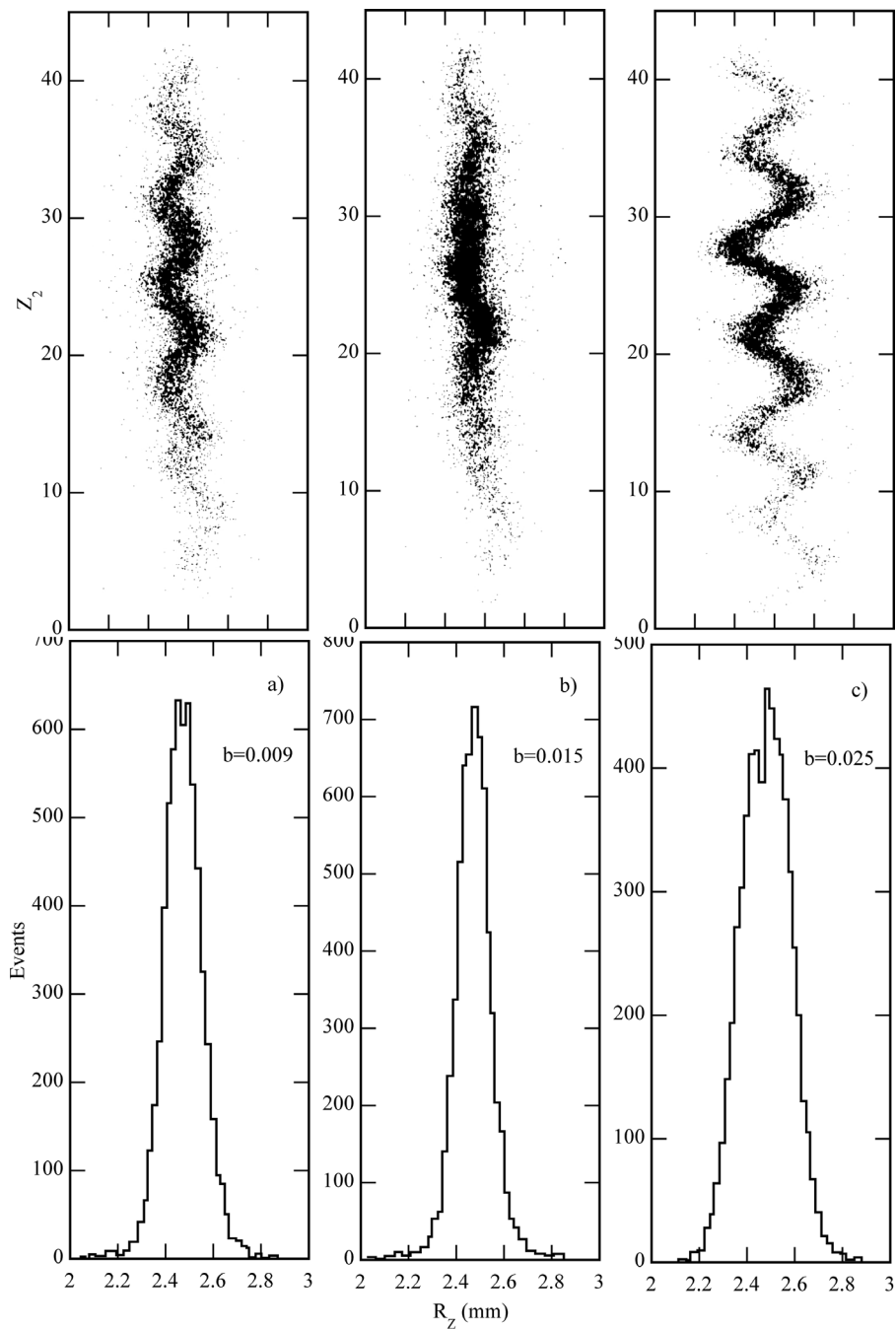


Figure 8.28 Localization accuracy along the anodes for three choices of the bias parameters (Piuz *et al.*, 1982). By kind permission of Elsevier.

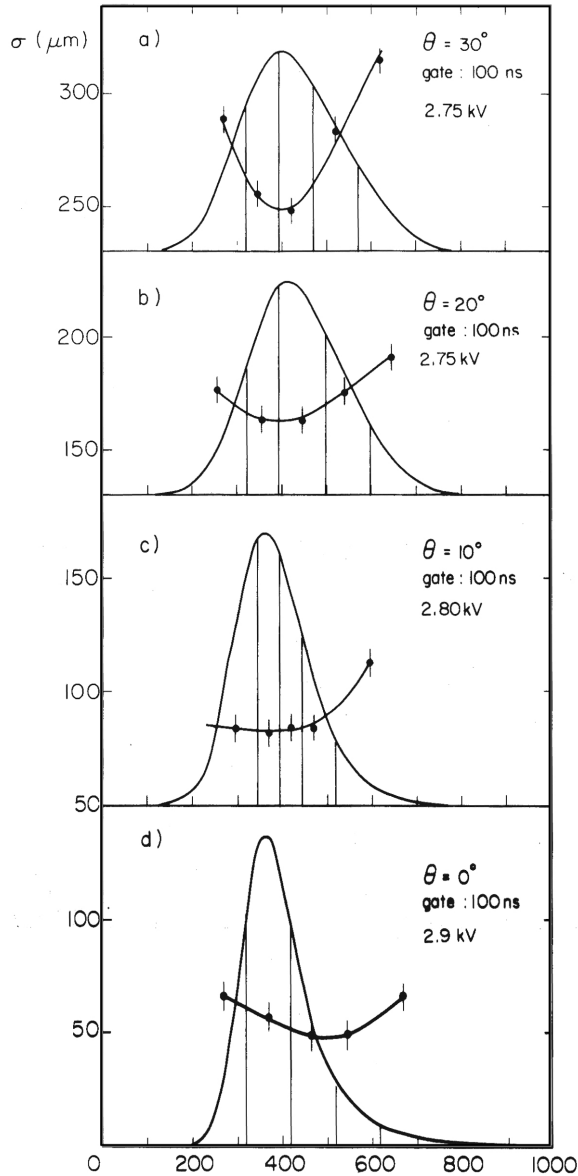


Figure 8.29 Localization accuracy as a function of energy loss for charged particles at different angles of incidence (Charpak *et al.*, 1979b). By kind permission of Elsevier.

Okuno *et al.*, 1979). Measured with a collimated ^{55}Fe X-ray source, Figure 8.33 is an example of the dependence of the avalanche width (FWHM) on the size, for several anode wire diameter (Fischer *et al.*, 1978). In the same references, the effects of varying the ionization density and the gas are also discussed. For small

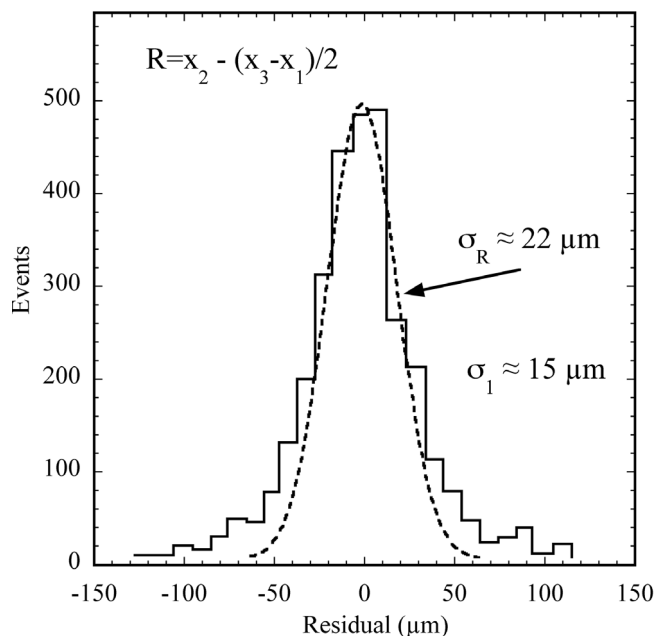


Figure 8.30 Residual distribution for 65 MeV protons perpendicular to three identical detectors. The single detector resolution is $15 \mu\text{m}$ rms (Bondar *et al.*, 1983). By kind permission of Elsevier.

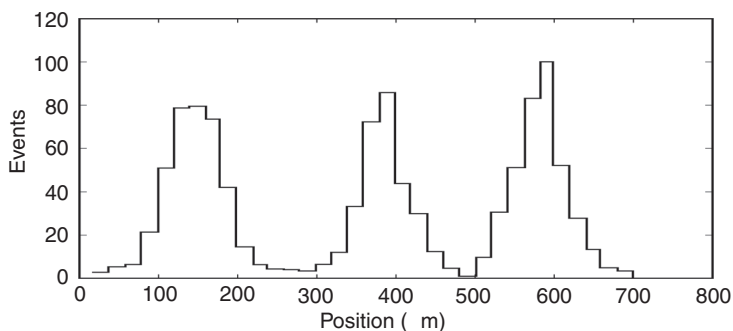


Figure 8.31 Centre of gravity position determination for three soft X-ray source position $200 \mu\text{m}$ apart in the direction of the anodes (Charpak *et al.*, 1978). By kind permission of Elsevier.

angular spreads, the difference in the signals induced on the two adjacent wires adjacent to the counting one can be exploited to resolve the right–left ambiguity, intrinsic in wire structures (Breskin *et al.*, 1977; Fischer *et al.*, 1978).

Aside from its relevance for optimizing the localization accuracy, the preferential production of positive ions along the direction of approach of the ionized trail



Figure 8.32 Two-dimensional X-ray image of a letter cut. The mask size is $4 \times 1.5 \text{ mm}^2$ (Charpak *et al.*, 1978). By kind permission of Elsevier.

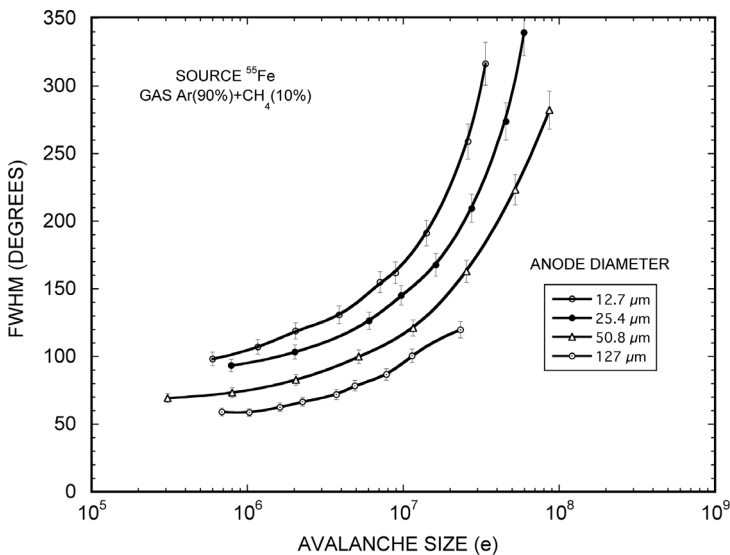


Figure 8.33 Avalanche angular spread as a function of size for several anode wire diameters (Fischer *et al.*, 1978). By kind permission of Elsevier.

affects other detector properties, as the fraction of ion feedback in time projection-like chambers (see Chapter 10).

Many authors have studied the shape of the avalanche-induced signals on anodes and cathodes in various geometries (Mathieson and Harris, 1978; Gatti *et al.*, 1979; Erskine, 1982; Chiba *et al.*, 1983; Gordon and Mathieson, 1984; Thompson *et al.*,

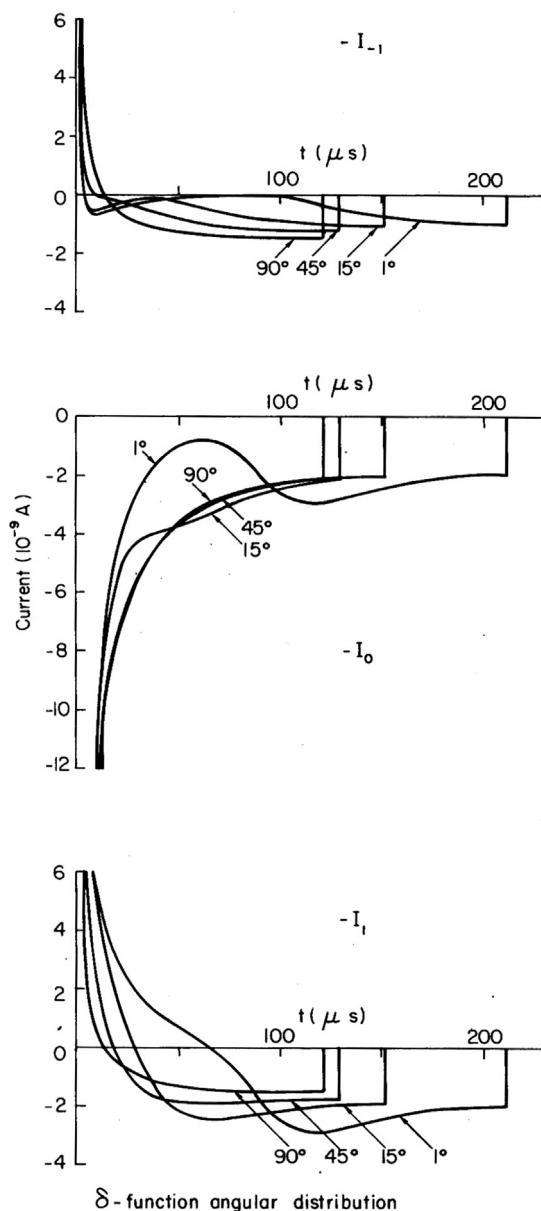


Figure 8.34 Computed signal current on three adjacent anode wires (Erskine, 1982). By kind permission of Elsevier.

1985; Staric, 1989; Landi, 2003; Riegler, 2004). Figure 8.34 and Figure 8.35 (Erskine, 1982) are examples of computed current and charge as a function of time on three adjacent anodes and on cathode strips, for a δ -function avalanche distribution centred at different angles (90° is perpendicular to the cathode planes).

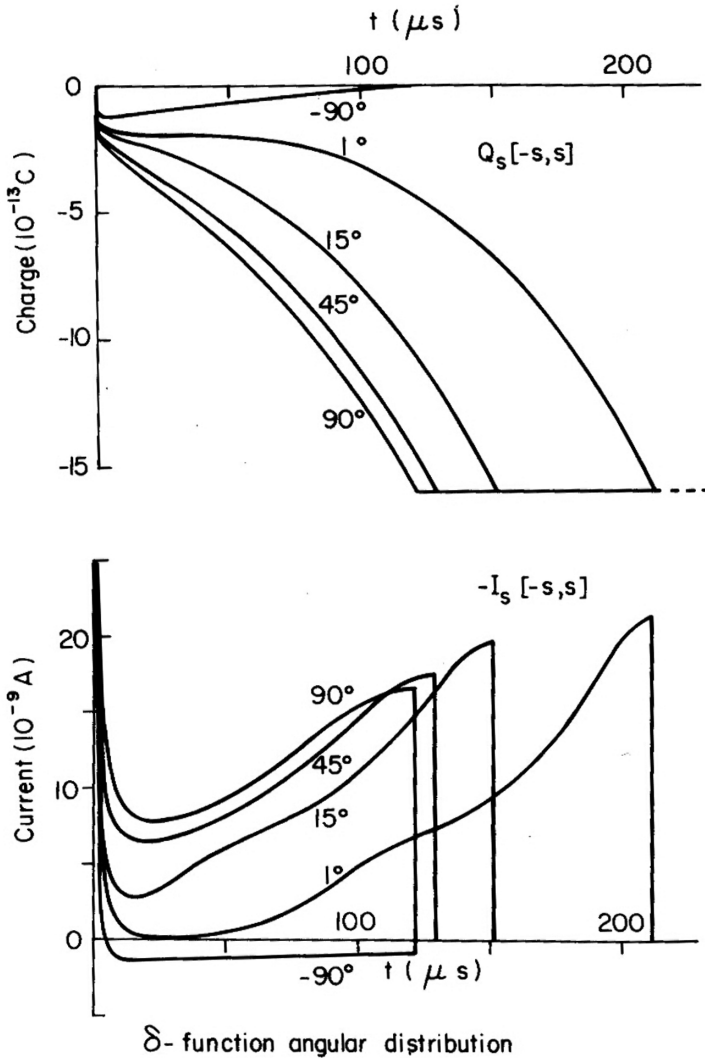


Figure 8.35 Computed induced charge and current on cathode strips facing the central anode wire (Erskine, 1982). By kind permission of Elsevier.

The resolution limits due to electronic noise and the optimum geometry for strip cathode readout are theoretically analysed in Gatti *et al.* (1979); it is found that the optimum ratio between the cathode sensing electrode width and the anode to cathode distance is about 1, a simple rule followed in most detectors.

With the introduction of the time projection chamber (TPC) (Nygren and Marx, 1978), the study of induced signals has been extended to devices with pad rows on the cathode plane, discussed in Chapter 10.

The induced charge readout method, while fully exploiting the MWPC performances, requires the implementation of a large number of electronic channels. Alternative methods of recording the two-dimensional coordinates of events has been introduced in the early developments of the detector, making use of electromagnetic delay lines, coupled to the signal electrodes, and inspired by similar systems used for the readout of wire spark chambers (Breskin *et al.*, 1974c). Variously manufactured with wire coils wound around an insulating core of rectangular cross section, the lines pick up the induced signals and transmit them with typical delays from a few to a few tens of ns/cm; an amplifier–discriminator circuit at each end of the line records the arrival time of the signals, thus providing the space coordinates after suitable calibrations. The limiting position accuracy achievable with delay lines depends on the ratio of signal rise time and delay; many authors have described optimizations of the design for best performances (Birk *et al.*, 1976; De Graaf *et al.*, 1979). While limited in rate capability and generally not able to disentangle multiple events, monolithic delay lines are a very cost-effective solution for moderate rate spectrometers (Breskin *et al.*, 1978; Atencio *et al.*, 1981), X-ray crystallography and biomedical imaging (Chechik *et al.*, 1996; Breskin 2000).

A lumped delay line, consisting of a multi-tap array of inductive delay cells capacitively connected to the detector cathode strips, permits one to achieve better localization and rate capability (Boie *et al.*, 1982). With a thorough optimization work on the components and of the front-end sensing electronics, the authors demonstrated in a small MWPC detector position accuracies better than 100 μm FWHM and integral non-linearity below 0.2%. Detectors based on this design have been used for high-rate X-ray synchrotron radiation experiments (Smith *et al.*, 1992).

A longitudinal localization method exploiting the current division on the two ends of the anode wires, originally introduced for the readout of MWPCs (Foeth *et al.*, 1973), has been developed mainly for the second coordinate readout in drift chambers, and is described in Chapter 9.

8.10 The multi-step chamber (MSC)

All detectors described so far have a single multiplication element, amplifying and detecting the ionization released in the gas. A double structure named the hybrid chamber, described in the early 1970s, consisted of a multiplication region delimited by wire meshes, transferring electrons into a second element, a spark chamber; the resulting delay permitted one to generate the high-voltage pulse used for triggering the main detector (Fischer and Shibata, 1972; Bohmer, 1973). The process leading to the transfer of a fraction of the electrons from a high into a low field region was, however, rather mysterious.

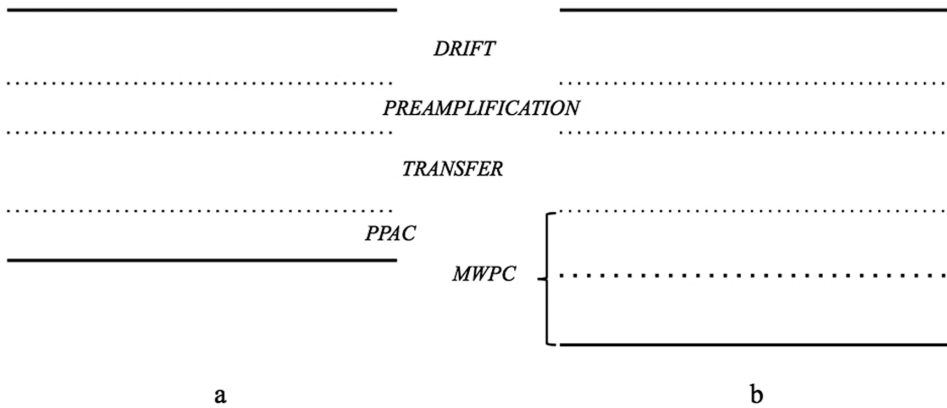


Figure 8.36 Schematics of the multi-step chamber with a parallel plate multiplier (a) and an MWPC as second amplification element (b).

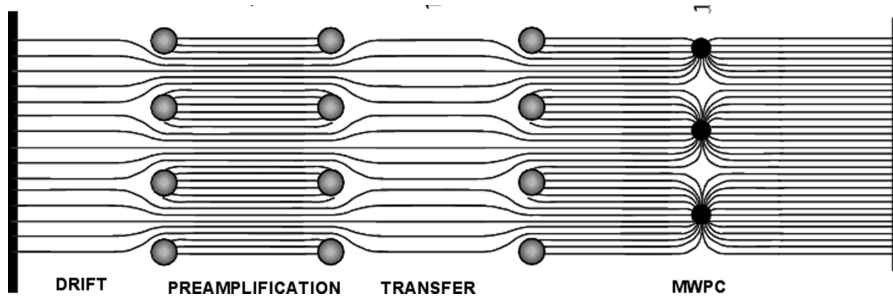


Figure 8.37 Electric field structure in the multi-step chamber with MWPC.

The pre-amplification and transfer mechanisms have been studied in the development of the multi-step chamber (MSC) (Charpak and Sauli, 1978). The structure has a high-field gap between two wire meshes, amplifying the ionization released and transferring a fraction of the electron avalanche through a transfer gap into a second element of amplification, parallel plate avalanche chamber (PPAC) or standard MWPC. Figure 8.36 shows schematically two possible implementations of the structure. Figure 8.37 is a schematic representation of the electric field lines in the second structure.

The picture in Figure 8.38 is an oscilloscope recording of the signals detected by irradiating the detector with a 5.9 keV X-ray source, converting in the drift region (Charpak and Sauli, 1978): the upper track corresponds to the pulses observed on the lower mesh of the pre-amplification gap, and has the shape expected from a negative charge multiplied and then leaving the electrode; the lower track corresponds to the delayed charge reaching the second amplification element. As seen in the picture, the energy resolution after transfer remains excellent. A measurement

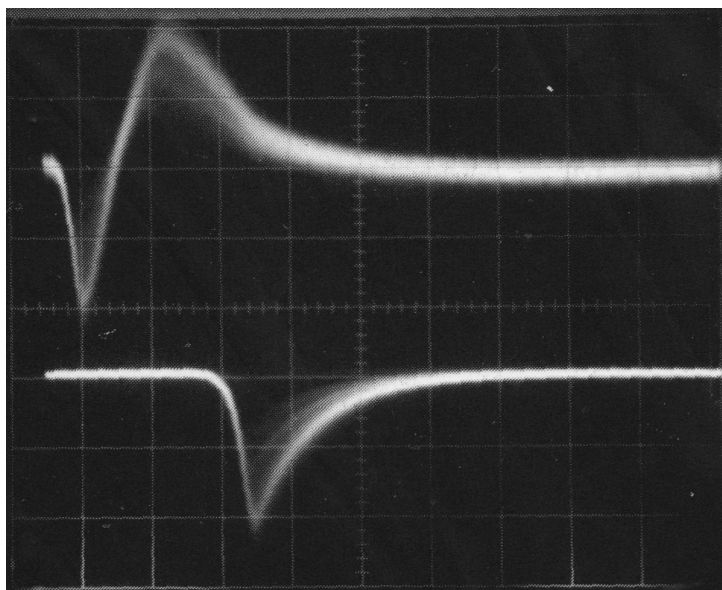


Figure 8.38 Prompt and delayed charge detected on the pre-amplification gap (top) and MWPC (bottom) (Charpak and Sauli, 1978). By kind permission of Elsevier.

of the ratio of transferred charge to the total avalanche size in the first amplification gap provides surprisingly large values of transfer efficiency, Figure 8.39; an example of total gains measured in a double step chamber with a PPAC main amplifier as a function of the voltage difference applied to the two multipliers is given in Figure 8.40 (Charpak and Sauli, 1978).

Developed initially with the aim of achieving large gains for the detection of UV photons emitted in a radiator by the Cherenkov effect, the early measurements were done using gas mixtures containing a photosensitive vapour, favouring an explanation of the observed large charge transfers based on a mechanism of UV photon emission and re-conversion in the gas. Further work demonstrated that the pre-amplification and transfer mechanism is effective in most gas mixtures and could be explained simply by the large lateral spread due to diffusion of the electrons multiplying in high fields.

Owing to the short absorption length of the additives, photons emitted in the final avalanche are reabsorbed before reaching the first multiplier, hence preventing feedback-induced divergence. Combining two amplification stages, gains in excess of 10^6 could be achieved with the MSC using photosensitive gas mixtures, permitting the detection and localization of single UV-generated photoelectrons. Figure 8.41 is an example of single electron pulse height spectra recorded at increasing gains, showing the evolution from exponential to a peaked Polya

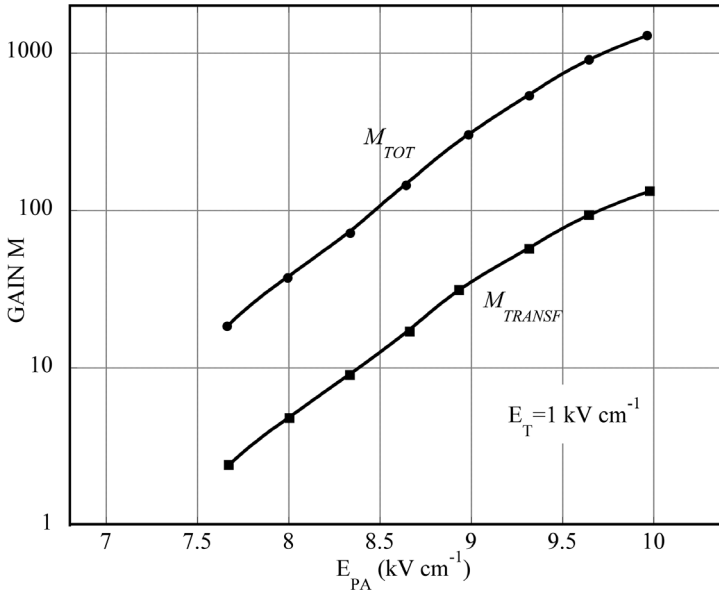


Figure 8.39 Total and transferred gain measured on the pre-amplification gap (Charpak and Sauli, 1978). By kind permission of Elsevier.

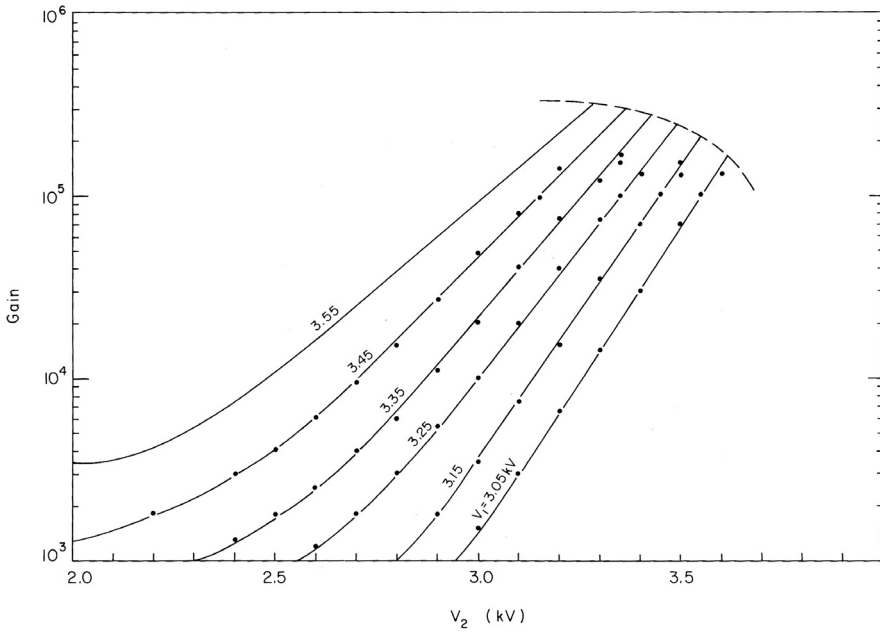


Figure 8.40 Total gain of a double parallel plate multi-step chamber as a function of voltages (Charpak and Sauli, 1978). By kind permission of Elsevier.

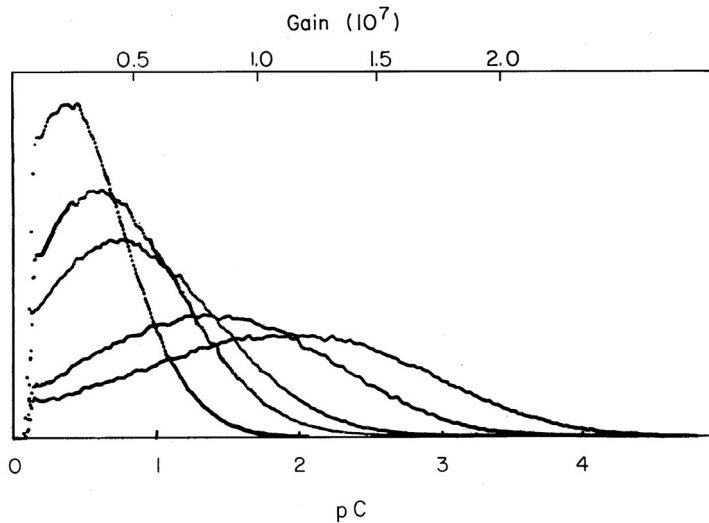


Figure 8.41 Single electron pulse height distributions recorded with a photo-sensitive multi-step chamber at increasing gains (Bouclier *et al.*, 1983). By kind permission of Elsevier.

distribution, as discussed in Section 5.4 (Bouclier *et al.*, 1983). This opened the way to application in ring imaging Cherenkov counters (RICH), described in Chapter 14. The gas electron multiplier (GEM) device, invented by the author (Sauli, 1997) and discussed in Chapter 13, is a reincarnation of the pre-amplification and transfer concept.

In a detector without the drift gap, thanks to the exponential multiplication characteristics of the pre-amplification element, the largest gain is obtained for ionization released close to the upper cathode, improving localization for low energy electron tracks, scattering in the gas; the principle has been exploited for imaging labelled anatomic samples in radiochromatography (Petersen *et al.*, 1980), and in the detection of thermal neutrons using converters (Melchart *et al.*, 1981).

8.11 Space charge and rate effects

The effect on gain of the positive space charge built up in proportional counters at high rates was discussed in Section 7.7. Since the gain reduction is a localized effect, extending perhaps one or two gap lengths around the hot spot in a chamber, substantial distortions in the detection can be induced if the rate limit is locally exceeded. Measurements of the average pulse-height as a function of rate in proportional counters were given in that section; the effect depends on the detector geometry and ion mobility, which can, however, not be varied over a very wide

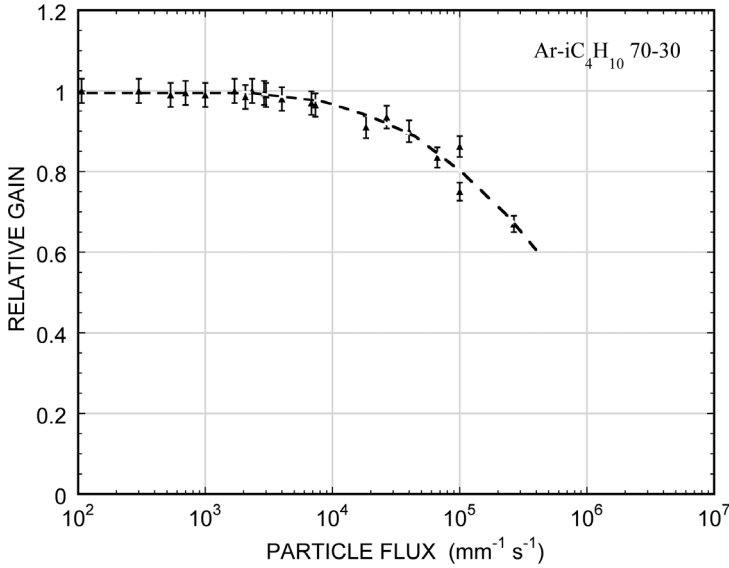


Figure 8.42 Relative gain as a function of rate measured with a drift chamber, normalized to the flux per unit wire length (Breskin *et al.*, 1974b). By kind permission of Elsevier.

range. For a given threshold of detection, inefficiency sets in when the lower part of the pulse-height spectrum distribution decreases below the threshold. High chamber gains and low thresholds are therefore needed for high rate full efficiency operation; in practice, however, at any given chamber gain the threshold value cannot safely be reduced below one tenth to one twentieth of the average pulse height, due to the noise generated by micro-discharges and other sources, and therefore almost identical efficiencies of detection versus rate have been measured in a large variety of gases and conditions.

Measured with a 50-mm anode wire spacing drift chamber, Figure 8.42 shows the gain as a function of minimum ionizing particle rate, expressed per unit length of wire (Breskin *et al.*, 1974b); Figure 8.43 provides similar measurements, realized with MWPCs having 1 mm and 0.64 mm wire pitches. Once normalized to the rate per unit length of wire, the results are consistent and show that the gain drops rapidly above a radiation flux of around 10^4 particles/mm of wire.

Depending on the electronics' detection threshold, the corresponding efficiency also drops at high rates. Figure 8.44 (Crittenden *et al.*, 1981) and Figure 8.45 (Breskin *et al.*, 1974b) compare the results of efficiency measurements for fast particles, realized with 1 and 2 mm pitch MWPC and with a 50-mm wire spacing drift chamber at several anode potentials; normalized to the rate per unit length of wire, the drop in efficiency is about the same, confirming the fundamental nature of the process, although the spatial extension of the positive charges may create some

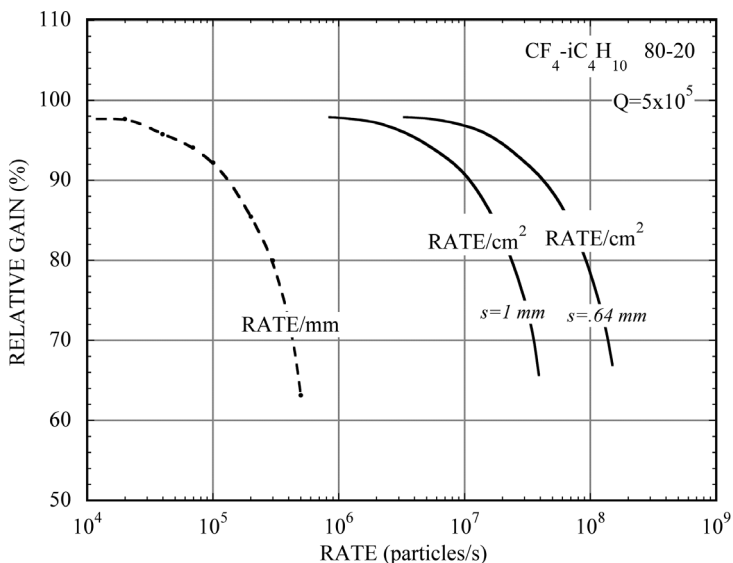


Figure 8.43 Relative gain as a function of rate for MWPCs with 1 mm and 0.64 mm wire spacing. Normalized to the flux per unit wire length, the two sets of data coincide (dashed curve) (Breskin *et al.*, 1974b). By kind permission of Elsevier.

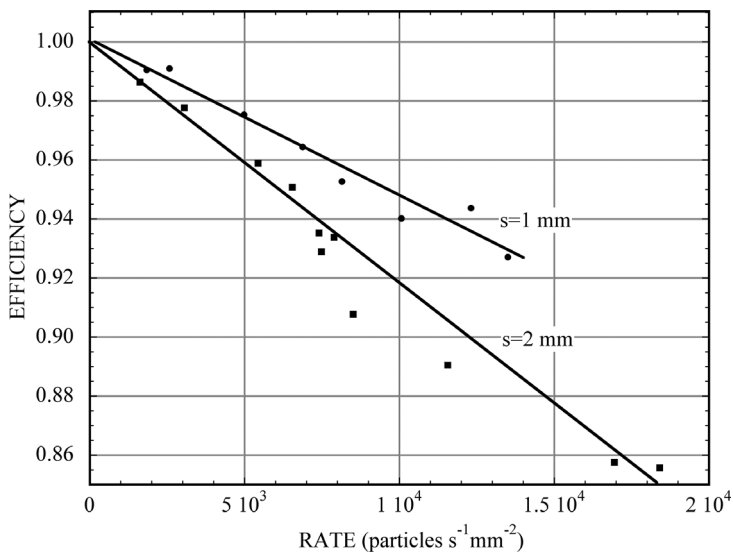


Figure 8.44 Efficiency as a function of particle rate measured in MWPCs with 1 and 2 mm wire spacing (Crittenden *et al.*, 1981). By kind permission of Elsevier.

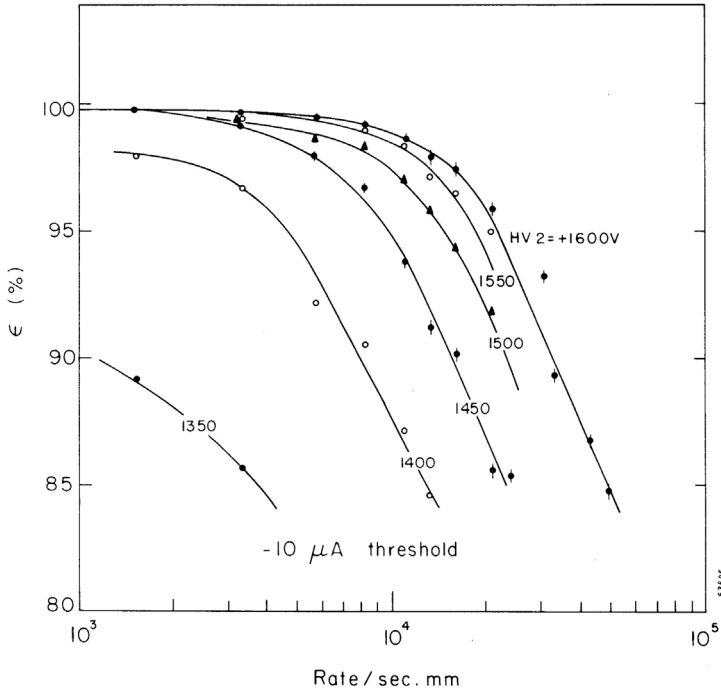


Figure 8.45 Detection efficiency of a 50 mm wire spacing drift chamber as a function of particle flux, given per unit length of wire, at several anodic potentials (Breskin *et al.*, 1974b). By kind permission of Elsevier.

degree of interdependence between close wires (see Section 7.7). Obviously, the larger wire pitch reduces the tolerable surface rate correspondingly.

Due to their impact on gain and space resolution in the ever-increasing experimental radiation fluxes, space charge field-distorting effects have been studied by many authors, both experimentally and theoretically. A modern mathematical formulation of the problem is discussed in Riegler *et al.* (2007).

As for proportional and Geiger counters, various processes of gradual deterioration under irradiation have been observed in MWPCs; depending on conditions, the degradation can be very fast, and has therefore been the subject of extensive investigations over the years. While a general solution to the ageing problems has not yet been found, a set of rules has been established to guide the experimenters in the choice of construction materials, operating gas and conditions; they will be discussed in detail in Chapter 16.

8.12 Mechanical construction of MWPCs

The basic problem for wire chamber construction is to support, on suitable frames, a succession of foils and wire planes constituting the electrodes, within strict

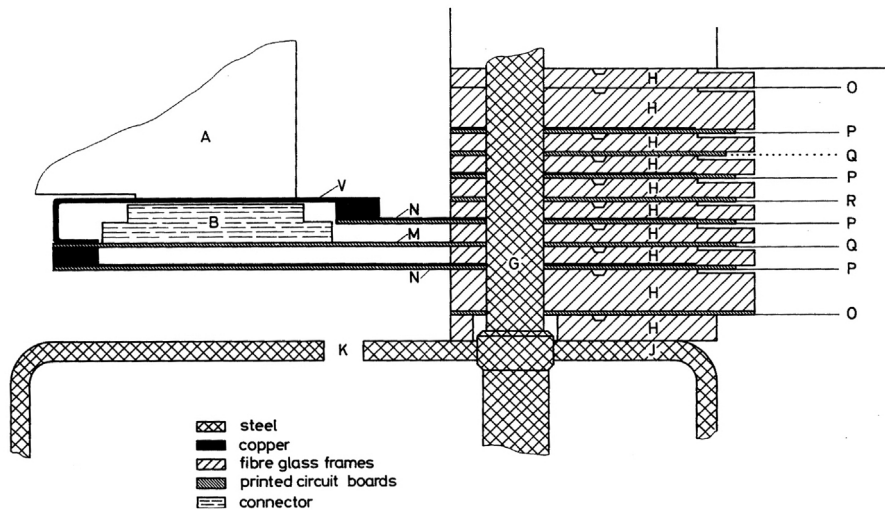


Figure 8.46 Schematic cross section of a MWPC frame assembly (Schilly *et al.*, 1970). By kind permission of Elsevier.

mechanical and electrical tolerances, and to make the whole structure gas tight and capable of sustaining the applied voltage. Several methods of construction have been developed; two representative examples are described here. The first, and more frequently used, consists of fabricating a set of self-supporting insulating frames, normally of extruded or machined fibreglass, one for each electrode. Wire planes are in general soldered on printed circuits pasted on the frames; a complete detector is then mounted either by gluing together the required number of frames (in the case of small chambers), or assembled with bolts and screws traversing the frames, the gas tightness being guaranteed by rubber joints (O-rings) embedded in the frames; thin gas-containment windows on the two outer surfaces complete the assembly. Figure 8.46 is a cross section of the frames used in the construction of the first large MWPC, and Figure 8.47 is a picture of the assembled detector used in a large aperture magnetic spectrometer experiment at CERN (Schilly *et al.*, 1970). A similar structure was used for a large MWPC prototype chamber developed by Charpak and collaborators, Figure 8.48 and Figure 8.49 (Charpak *et al.*, 1971). A photograph of the fully assembled detector was shown in the introduction (Figure 1.6), and is also the first known picture of Georges Charpak with a MWPC. A close view of the frame with the anode wires soldered on a printed circuit board, providing the connection to the readout electronics, is shown in Figure 8.50.

A drawback of the described technique lies in the rather unfavourable ratio between active and total detector surface. In cases where the detection volume is

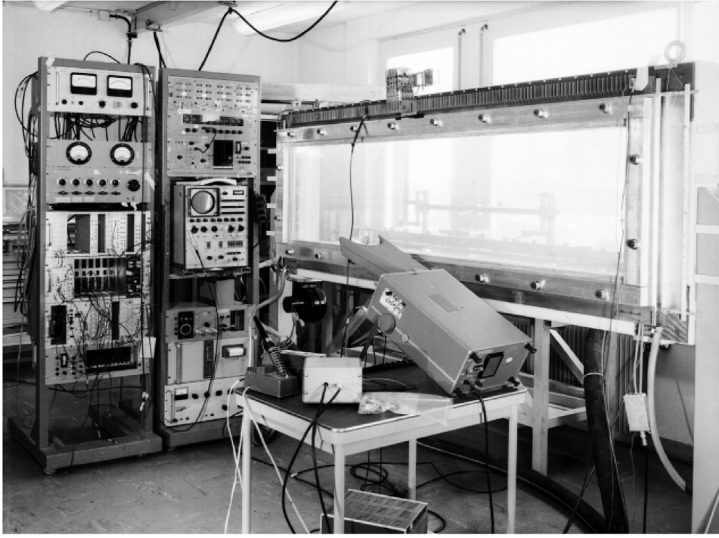


Figure 8.47 The first large MWPC (Schilly *et al.*, 1970). By kind permission of Elsevier.

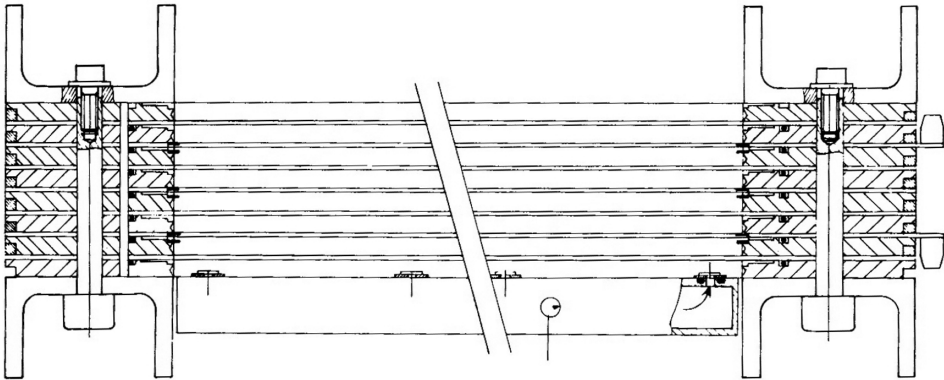


Figure 8.48 Cross section of a three-wire plane MWPC framing (Charpak *et al.*, 1971). By kind permission of Elsevier.

limited, as inside a magnet, the loss is considerable. For this reason, a different construction principle has been developed, based on the use of metal-coated self-supporting honeycomb or expanded polyurethane plates, which constitute both the cathode planes and the mechanical support of the chamber. A schematic of such self-supporting chambers is shown in Figure 8.51 for a twin-gap MWPC; narrow insulating frames (one cm or less), on which the anode wires are stretched and soldered, are glued along edges of the plates (Bouclier *et al.*, 1974). The fishbone

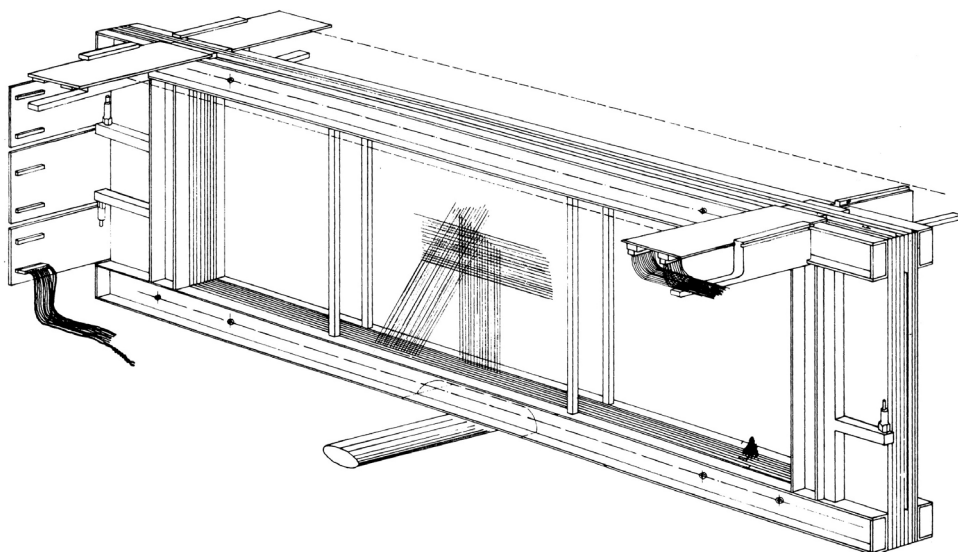


Figure 8.49 Assembled large MWPC prototype (Charpak *et al.*, 1971). By kind permission of Elsevier.

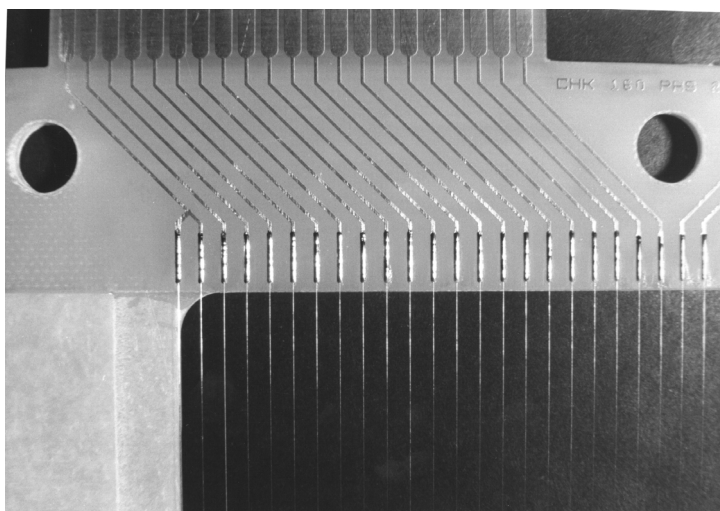


Figure 8.50 Close view of the anode wires soldered to a printed circuit board. Picture by the author (1973).

structure of the strips in the cathode plane, used to provide coarse information on the tracks' second coordinate, is also visible. The honeycomb-based structural construction has the advantage of being light, and can be tailored to particular requirements of the experiment: in the example, the structure is shaped to allow

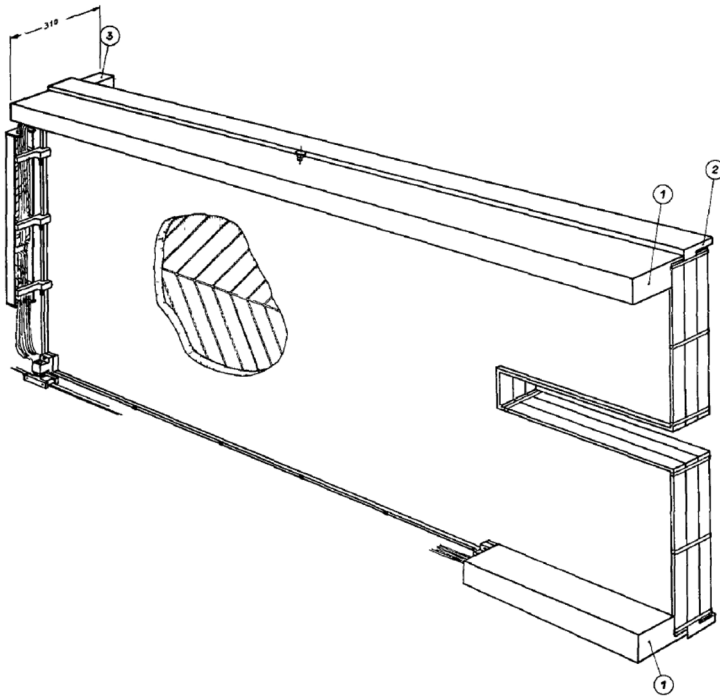


Figure 8.51 Light MWPC construction, making use of expanded polyurethane plates and thin frames for holding the anode wires (Bouclier *et al.*, 1974). By kind permission of Elsevier.

assembly around the beam vacuum tubes (in this case the CERN intersecting storage rings). The obvious advantages of a large active area and ease of construction are counterbalanced by a rather substantial increase in the chamber thickness in the active area ($\sim 0.6 \text{ g/cm}^2$ against a few mg/cm^2 for a conventional thick-frame construction).

A picture in the introduction (Figure 1.7) shows the 40-chambers system, built with self-supporting chambers as described, installed in the split field magnet detector at CERN's intersecting storage rings and operated for many years. A similar self-supporting construction was used for the external MWPC system providing particle identification at CERN's big European bubble chamber (Brand *et al.*, 1976).

Systems of large MWPCs named cathode strip chambers (CSC) are used for triggering and localization in the CMS end-cap muon detector at CERN's LHC. Built with sizes up to $3.4 \text{ m} \times 1.5 \text{ m}$, the chambers have rigid supporting cathode planes manufactured with copper-clad, 1.6 mm thick fibreglass plates; radial readout strips are milled directly on the panels (Acosta *et al.*, 2000; Ferguson *et al.*, 2005). While a single layer time resolution is not sufficient to identify the

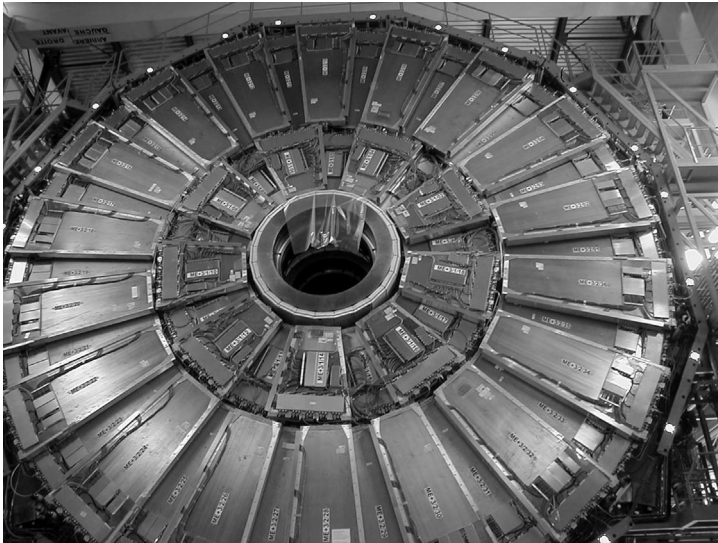


Figure 8.52 Cathode strip chambers array for the CMS muon end-cap. Picture CERN (2007).

bunch crossing,⁵ this is achieved by a hardware selection of hits on several aligned planes. Off-line analysis of the charge profiles recorded on cathode strips can provide the track position with sub-mm accuracy (Barashko *et al.*, 2008). A long-term irradiation of the detectors has demonstrated their survivability in the LHC harsh radiation environment (Acosta *et al.*, 2003). The picture in Figure 8.52 shows one layer of the cathode strip chambers system built for the CMS muon end cap detector.

As discussed in Section 8.4, for large detector sizes, wire instabilities and overall electrode deflections take place, degrading the operation, unless suitable mechanical support lines are used to balance electrostatic forces. Supports must be insulating if in contact with the anodes and, because they have a dielectric rigidity different from the gases, the local field modification affects the detection efficiency over a large area, a centimetre or so, around the support. The measured local efficiency drop in the region of a thin insulating wire support, perpendicular to the anode wires, is shown in Figure 8.53 (Schilly *et al.*, 1970).

Other support methods have been developed, in which an insulated wire or a conductive strip, close to the anode wires but not in contact with them, is raised to a potential high enough to, at least partially, restore the field and therefore the efficiency of detection. Figure 8.54 is an example of a vinyl-insulated support line and of the corresponding local efficiency measurement (Charpak *et al.*, 1971); the

⁵ The time between collisions at LHC is 25 ns.

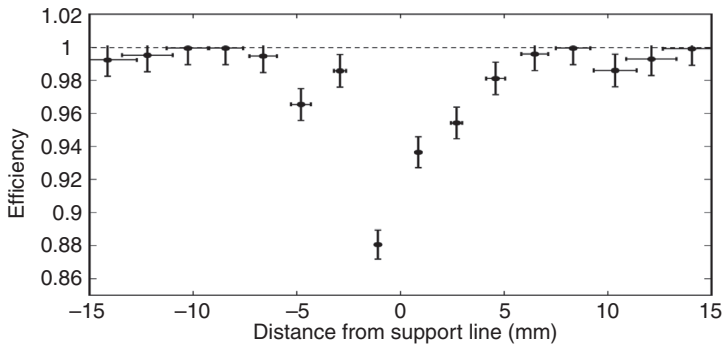


Figure 8.53 Local inefficiency induced by a thin insulating support line in contact with the anode wires (Schilly *et al.*, 1970). By kind permission of Elsevier.

picture in Figure 8.55 shows a corrugated thin kapton strip, or garland, compensating both for the anode wire instability and for the gap squeezing due to electrostatic forces (Majewski and Sauli, 1975). The structure has been used by many groups in the construction of large size multi-wire and drift chambers (Bozzo *et al.*, 1980; Hammarström *et al.*, 1980a; De Palma *et al.*, 1983).

A comparison of construction methods and materials can be found in Veress and Montvai (1978); the note also provides numerical evaluations of the frames' deformations caused by the stretched wires for several structures.

Methods for mounting wires on the chambers' frames are mainly of three types: manual stringing, weaving machines and turn-wheel sprockets; such systems have been developed by the engineering support groups in various laboratories. The simplest, used for prototype construction or small quantities, consists of stringing by hand one wire after the other over a horizontal frame, keeping the tension with appropriate weights placed at one or both ends, and soldering the wires to printed circuit boards. The desired wire distance is obtained with the use of external reference marks or light saw-tooth-shaped rules placed over the wire mesh. An example of manual construction can be found in Staric *et al.* (1983). Limited to small productions, the method is often used for repairing defective wires.

More sophisticated, and with a conception close to their industrial siblings, dedicated winding machines have been built having a motor-driven flying chariot with a wire feeder travelling between the two sides of a heavy frame. Wires are stretched between two comb-shaped racks with teeth at the desired pitch; a stepping motor and a wire tensioning system ensure the correct position. Once the full wire plane is woven, it can be directly soldered to the final frame, or fixed to a temporary transfer frame for later assembly. Description of such wire stretching systems can be found in Alleyn *et al.* (1968) and Bock *et al.* (1994).

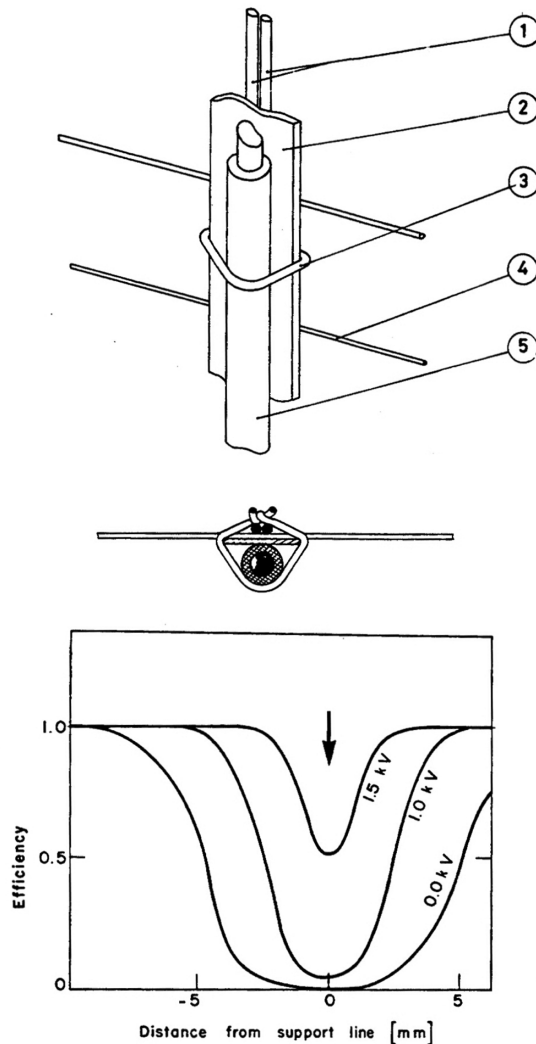


Figure 8.54 Support line with field-restoring insulated wire. With a suitable potential applied, the inefficiency loss is limited to a few mm (Charpak *et al.*, 1971). By kind permission of Elsevier.

The pictures in Figure 8.56 and Figure 8.57 are examples of waving machines of this kind used at CERN for the construction of wire chamber planes.

An alternative wiring method consists of a spinning frame, planar or cylindrical, rotating on an axis perpendicular to the wire feeder; a stepping motor, synchronized with the frame, ensures the desired wire pitch. To avoid breaking the wires during weaving, the mechanical tension is usually only a fraction of the one required; the final tension is obtained with the use of stretchable transport frames.

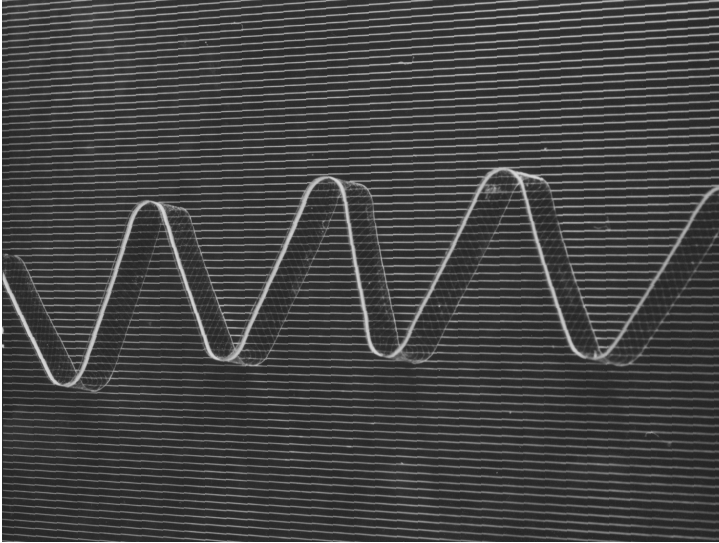


Figure 8.55 Corrugated kapton strip (garland) used for gap restoring (Majewski and Sauli, 1975). By kind permission of CERN.



Figure 8.56 Close view of a winding machine at CERN. Picture CERN (1975).



Figure 8.57 A wire winding machine used at CERN for the construction of the NUSEX chambers. Picture CERN (1981).



Figure 8.58 A rotating frame winding machine used for the wiring STAR TPC MWPC modules. Courtesy Brookhaven National Laboratory (USA).

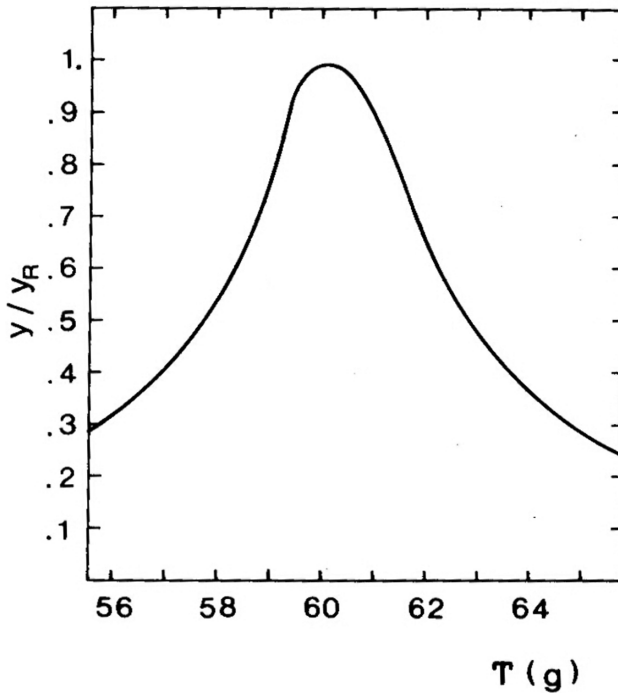


Figure 8.59 Relative resonance frequency of a wire, 1 m long, as a function of mechanical tension (Borghesi, 1978). By kind permission of Elsevier.

A system of this kind, making use of an octagonal drum, is described in Cavalli-Sforza *et al.* (1975). The picture in Figure 8.58 shows a wire weaving rotating frame used at BNL for the construction of the STAR TPC end-cap multi-wire modules. A simple table-top automatic winding and wire-soldering machine are described in Martinez *et al.* (2007).

To avoid electrostatic instability problems, after fabrication of a wire plane, it is advisable to check value and uniformity of the mechanical tension of each wire. For small detectors, a simple method consists of measuring the wire's sagging with a small weight gently put down in the centre of each wire. More sophisticated mechanical resonance systems rely on finding the natural frequency of oscillation of the wires, excited by an oscillator coupled through a metal foil or plate placed parallel to the wire plane; the resonance can be enhanced by an external magnetic field (Borghesi, 1978; Regan, 1984; Bhadra *et al.*, 1988; Mueller, 1989). Figure 8.59, from the first reference, gives an example of relative resonance frequency as a function of tension for a wire 1 m long.

Further reading

- Charpak, G. (1970) Evolution of the automatic spark chambers, *Ann. Rev. Nucl. Sci.* **20**, 195.
- Sauli, F. (1977) *Principles of Operation of Multi-wire Proportional and Drift Chambers* (CERN 77-09).
- Charpak, G. and Sauli, F. (1984) High-resolution electronic particle detectors. *Ann. Rev. Nucl. Part. Sci.* **34**, 285.